Journal of Engineering Advancements

Editor-in-Chief:
Prof. Dr. Mohammad Mashud

Volume 03 Issue 04

Journal of Engineering Advancements

Dr. Zahir Uddin Ahmed
Khulna University of Engineering & Technology
Email: zuahmed@me.kuet.ac.bd

Dr. Mohammad Ilias Inam
Khulna University of Engineering & Technology
Email: iliasinam@me.kuet.ac.bd

Dr. Md. Mahfuz Sarwar
AECOM
Email: mahfuzsarwar@yahoo.com

Dr. Md. Abdullah Al Bari
University of Calgary, Canada
Email: mdabdullahal.bari@ucalgary.ca

Dr. Shehata Eldabie Abdel Raheem
Assiut University
Email: shehataraheem@gmail.com

Dr. Smita A Francis
Namibia University of Science and Technology
Email: smitafrancis@gmail.com

Dr. Riaz U. Ahmed
University of Wisconsin-Green Bay
Email: ahmedm@uwgb.edu

Dr. Kazi Mostafijur Rahman
Khulna University of Engineering & Technology
Email: mostafij@me.kuet.ac.bd

Dr. Md. Rashedul H. Sarker
University of Indianapolis
Email: sarkerm@uindy.edu

Dr. Md. Najmul Hossain
Pabna University of Science & Technology
najmul_eece@pust.ac.bd

Dr. Yakubu Ajiji Makeri
King Ceasor University
Email: icydtorg.ug@gmail.com

Journal of Engineering Advancements

CONTENTS

Original Articles

Journal of
Engineering Advancements

Editor-in-Chief

Prof. Dr. Mohammad Mashud

Department of Mechanical Engineering,
Khulna University of Engineering & Technology, Khulna, Bangladesh

Executive Editors

Prof. Dr. Md. Shariful Islam

Department of Mechanical Engineering,
Khulna University of Engineering & Technology, Khulna, Bangladesh

&

Prof. Dr. Md. Arifuzzaman

Department of Mechanical Engineering,
Khulna University of Engineering & Technology, Khulna, Bangladesh

This page is left intentionally blank

A GUI-Based Peg-Free Hand Geometry Recognition for Biometric Access Control using Artificial Neural Network

Kazeem B. Adedeji [a,] and Oluwatimilehi A. Esan [b]*

[a]Department of Electrical and Electronics Engineering, The Federal University of Technology, Akure, Ondo State, Nigeria
[b]Department of Computer Engineering, The Federal University of Technology, Akure, Ondo State, Nigeria

ABSTRACT

Hand geometry has been a widely used biometric authentication because it is generally believed that the human hand has sufficient anatomical features which could be used for personal identification. Many hand geometry systems use pegs, which guide hand placement on the scanner. The system prompts the user to position the hand on the scanner several times and only captures when the current position is satisfied. In such a system, measurements are not very precise and this reduces accuracy during feature extraction. The system also has a higher false acceptance rate. This paper presents a peg-free hand geometry recognition system that does not depend on the orientation of the hand. Several features from test hand images are extracted and stored in the database, which are used to train an artificial neural network (ANN). To facilitate easy usage of the hand geometry verification system (peg-free), a GUI was developed using MATLAB software. The developed system was validated and the overall result shows that the system can be used for biometric verification using hand geometry where the orientation and placement of the hand are not a necessity. The results show that the developed system performed better with a relatively low false acceptance rate and false rejection rate of 0.01% and 0.02% respectively. The system also has a lower mean square error of 8.84×10^{-5}.

Keywords: Access Control, Artificial Neural Network, Biometric, Hand Geometry, Security.

1 Introduction

The fight against insurgence and combating cyber security has been the focus of nearly all countries nowadays. One way to combat security issues is to have the biometrics of every individual accessing a resource, which could be physical or cyber. Thus, personal identification for access control becomes increasingly vital in the quench of security. In the past and recent years, biometric-based identification systems have been used to provide an automated means of recognizing individuals based on their physiological and behavioural features [1]. A plethora of human anatomical features have been used for biometric systems. As presented in Figure 1, some of these include the use of fingerprints, face, iris, retina, voice, handwritten, face thermogram, hand geometry recognition, palm vein, and DNA matching [2]-[15]. In facial recognition systems (Fig. 1(a)), the position of some parts of the face is analysed to find a match [4]-[7]. Unfortunately, this system has some limitations. One of the limitations is that its major focus is the face (hairline down) and, consequently, the user may have to look straight at the camera before recognition could be possible. In the fingerprint recognition system (Fig. 1(b)), an optical sensor is utilized to capture line patterns on the finger, which are then analyzed. In the practical sense, some line patterns on the finger surface are so similar that it makes classification a difficult task. Thus, a high false acceptance rate is a common feature of this system. The use of iris recognition (Fig. 1(c)) for biometrics has also been reported [8], [9]. When an iris scan is performed, some features within the iris are captured, and they are then transformed into a bar code. This system has been an excellent security technique when used for biometric identification. However, a major problem with this system is the resistance from the users. The user needs to be in

a good position for the scanner to read the iris. In most cases, it irritates the user. Another technology is the palm vein recognition system [11]–[13]. As shown in Fig. 1(d), it involves identifying some vein patterns on the palm. The speed at which the scanning is performed is relatively faster and more accurate. The system also provides some level of user convenience. However, it is costly. Therefore, the system is seldom used, although it could be used in applications where the security demand is vital. In hand geometry systems [16]-[19] (Fig. 1(e)), a fusion of the hand and palm features were used for personal identification.

Amongst the biometric recognition systems, the hand geometry system is frequently used due to the fact that the verification process is straightforward [20]–[26]. In this system, some features, which include shape, palm size, length, and width of the fingers, are extracted from the human hand. It has been reported that the hand features of humans are distinctive [1], [19] and after a certain age, a person's hand does not alter considerably. Unlike other biometric systems, during the dry season when some individuals experience dry skin, the accuracy of the verification process is not negatively affected [19]. Likewise, other biometric traits require exclusive scanners for data collection. However, hand images may be obtained using a low-cost webcam or digital camera. These, amongst other features, make the hand geometry-based system a widely accepted biometrics system for access control. Many hand geometry systems use pegs, which guide the hand's placement on the scanner. The system prompts the user to position their hand on the scanner several times and only takes an image of the hand when their current position is satisfied. In such a system, measurements are not very precise and this reduces accuracy during feature extraction.
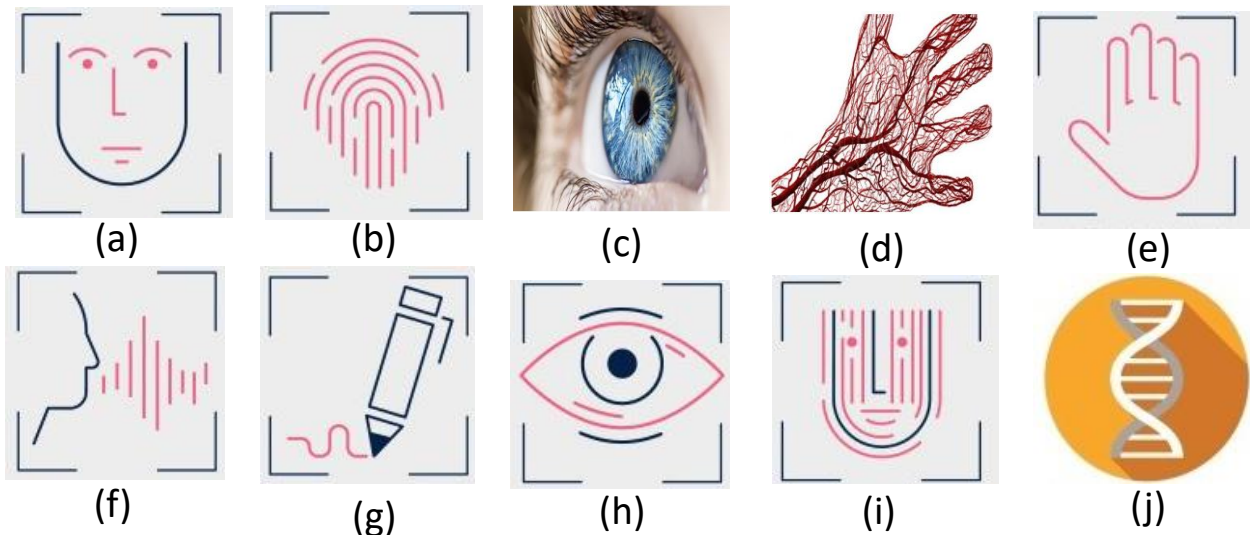
Fig. 1 Human traits used for biometric recognition (a) face recognition (b) fingerprint (c) iris recognition (d) palm vein recognition (e) hand geometry (f) voice recognition (g) hand written (h) retina recognition (i) face thermogram (j) DNA matching.

Thus, a system that is independent of the hand orientation is vital which is the focus of this study. Several research studies in this domain have been presented [19]-[35] with different levels of success in terms of false acceptance and rejection rate. This paper aims to improve the existing system and present a much deeper analysis of the biometric identification system. The paper is organized as follows: Section 2 presents a review of some related studies and the main contribution of this paper. Section 3 describes the system architecture and the ANN implementation. In section 4, the results of the implementation of the peg-free system are discussed, while section 5 concludes the paper and presents future work.

2   Review of Related Studies and Contributions

Several review studies on hand geometry recognition systems are available in the published literature with different levels of success. In [19], an innovative peg-free hand-geometry-based user identification system was proposed. The system uses spectral properties of a minimal edge-connected graph representation of the hand image. In this study, a multiclass support vector machine (MSVM) is employed to identify the claimed user. The applicability of the proposed system was demonstrated on two databases, namely the GPDS150 hand database and the VTU-BEC-DB multimodal database. The system achieves relatively better identification with a false rejection and false acceptance rate of 2.05% and 0.69%, respectively. Boreki and Zimmer [27] present a control access system based on hand geometry, a hardware key, and a vital sign detector. The features of the hand images are extracted using the analysis of the curvature profile of the image. This makes the proposed system invariant to the rotation and translation of the hand. The system achieves a relatively low false acceptance rate (0.8%) when demonstrated on a database having more than 360 hand images. Adan et al. [28] presented a hand biometric system for verification and recognition using a Natural Reference System (NRS). In this work, the hand's features are obtained through the polar representation of the hand's contour, which allows the study to achieve a minimum image processing and low computational

cost. The system achieves a good false acceptance rate and false rejection rate of 0.45% and 3.04%, respectively when demonstrated on 5640 images that belong to 470 users. In Villegas et al. [29], wavelet features from the nearest neighbour were used to achieve biometric hand geometry identification. In this study, an input image of a hand was obtained using a scanner; the image was pre-processed and transformed to the wavelet domain. The stage of classification is performed using a simple nearest neighbour algorithm with Euclidean distances. The applicability of the system was verified using a database having 120 hand images. The system achieves a recognition rate of 70.2 with a false rejection rate of 10.4%.

Several other studies in this domain have been observed to use different classifiers for biometric identification using hand features. In [30], a hand geometry identification system was presented using a geometric classifier with a good false acceptance rate of less than 1%. In [31], a peg-free hand geometry measurement was utilized for human identification. A false rejection rate of 1% was obtained in this study. The authors [32] utilize neural networks for biometric hand recognition. The study uses 2800 hand images to train and verify the proposed system with a relatively low false rejection rate of 0.148%. In [33], a fusion of 2D and 3D hand geometries was used for biometric verification. The system uses a database consisting of 120 hand images and achieves a relatively high false rejection rate and the false acceptance rate of 10.4% and 11.4%, respectively. Polat and Yildirim [34] use a general regression neural network for hand geometry identification. A database consisting of 140 hand images was used to train and validate the system. The proposed system achieves a high false acceptance and false rejection rate of 15%. This could be due to the fact that the features of the hand images were not extracted before the identification stage; thus, a high false acceptance rate is expected. The work proposed by [35] presents a hand geometry user identification algorithm that utilizes data acquired by a standard office scanner. During verification, a false acceptance rate and a false rejection rate equal to 0.0% and 1.19% were obtained. However, during identification, a different result was reported.

At this stage, the results showed that the false acceptance rate was superb (0.0%) while the false rejection rate was 1.19%. Iula [36] utilizes a 3D ultrasound hand geometry for biometric recognition. In this study, several 2D images are first extracted at increasing under-skin depths, and from each of them, up to 26 distances among key points of the hand are defined and computed to achieve a 2D template. A 3D template is then created by combining two or more 2D templates in various ways. The performance of the proposed system was verified using a homemade database. The results presented revealed that good recognition accuracy was achieved. This study was improved in [37] with an identification rate of 100%.

Based on our examination of the existing literature studies in this domain, it is observed that a different level of success has been achieved. Aside from the study in [35] that achieved a superb performance in terms of the false rejection rate (though during only the identification stage and not the entire system), we observe that improving the false acceptance and rejection rate for the entire system is vital. This paper aims to improve the existing system, presents a much deeper analysis of the biometric identification system, and motivates the research scholar to become personally involved in an effort to improve biometric recognition through hand geometry identification.
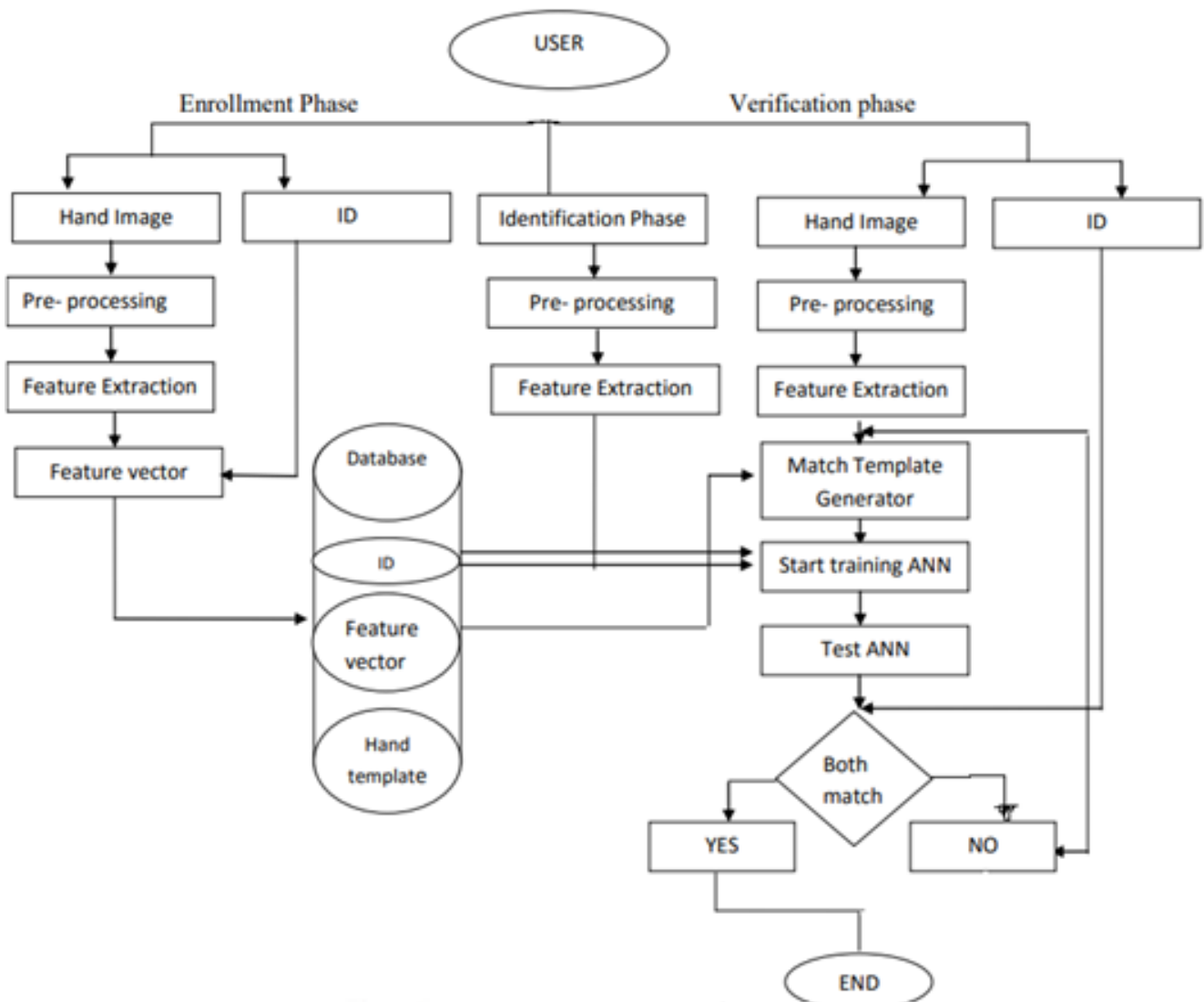
Fig. 2 The architecture of the developed hand geometry system.

3 System Architecture

The architecture of the developed hand geometry is shown in Fig. 2. The system was implemented to control the access of undergraduate students to a lecture hall in a tertiary institution. It consists of enrolment, identification, and verification. In the enrolment stage, data is collected using a CCD camera and then delivered to a feature extractor, which converts the data into numerical features. The feature extraction is done through Harris corner detection, which detects corner points in the image. It first finds the difference in intensities for the displacement of features over a window size. The output of the feature extractor was added to the database as a saved template marked with a user identity.

At the identification stage, the images are marked with an ID, which is classified into classes and also to a formulated timetable as shown in Table 1.

Table 1: Rule-based access control for computer engineering undergraduate students in a tertiary institution

ID	Rule Basis	Policy Rules for Access	Result/Output
1-50	300 level Students	Monday's:8am-12pm Tuesday's:12pm-4pm Wednesday's:8am-12pm	Grant access if ID 1-50 match with the trained features
51-100	400 level Students	Wednesday's:12pm-4pm Thursday's:8am-12pm Friday's:8am-12pm	Grant access if ID 51-100 match with the trained features
101-150	500 level Students	Modays's:12pm-4pm Tuesday's:8am-12pm Friday's:1pm-4pm	Grant access if ID 101-150 match with the trained features

A matcher gets the stored templates relating specifically to claimed usernames during the verification step. The similarity between an input feature and the recovered template is determined using a distance measure. The system approves if the distance is less than a predetermined threshold; otherwise, it refuses. The operations involved in each of these stages are discussed in the next section of this paper.

3.1 Enrolment Phase

3.1.1 Image Acquisition

Images are obtained from the College of Engineering Pune Palm Print database, which consists of the right-hand images acquired through the use of a digital camera, each with 5 pixels. A colour or grayscale image of the hand palm is used as the input. For image processing, the images are stored in the Joint Photographic Experts Group (JPEG) format in the database. Fig. 3 shows samples of the hand images.

Fig. 3 Samples of the captured hand images.

3.1.2 Pre-processing

(A) Grayscale image conversion

It is observed that the original image is coloured, and must be converted to grey-scale images using the r2bgray function. This function cancels the huge saturation information in the image while keeping the luminance information. Each pixel in a grayscale image has a single sample value. After converting the image to grayscale, a threshold is determined and the image is transformed into a binary image. In a binary image, all pixels in the input image with intensity above 1 have a value of 1 (white), and 0 (black) otherwise. Thus, at a certain threshold T, the transformation of an input image A into a binary image B can be represented as

$$B_{ij} = \begin{cases} 1 & for \quad A_{ij} > T, \\ 0 & otherwise \end{cases} \qquad (1)$$

where i denotes images 1,2,3,..,149, j is the last image, B_{ij} =1, for the object or background pixels, and B_{ij} =0, for the background images. The process of image binarization divides pixel values into two groups: background pixels and foreground or object pixels. During the feature extraction process, image binarization aids in the extraction of minute details [17]. Thus, when input image (i, j) ≥ threshold, the output image (i, j) =1, however, if input image (i, j) < threshold, the output image (i, j) = 0.

(B) Noise removal

Noise in the image must be removed since it can cause a disparity between the actual palm and the captured image. Another reason for noise removal is that edge detection in noisy images is challenging due to the high-frequency content of both the noise and the edges. Each image has two major constituents, as shown in Eq. (2) [16].

$$L'(x,y) = L(x,y) + N(x,y) \qquad (2)$$

where L' denotes the noisy image, L denotes the actual image, N is the noise component, and x, y denote pixel coordinates. In MATLAB, Wiener2filter is used to eliminate the noise. Therefore, measuring the noise level in an image becomes vital. This can be accomplished using the signal-to-noise ratio (SNR). The higher the SNR value, the better the image quality [16]. It is possible to evaluate the SNR in an image using Eq. (3).

$$SNR(L, L') = 10log(\sigma^2(L)/MSE(L, L'))$$ (3)

where σ^2 is the image variance, MSE is the mean square error. Also,

$$MSE(L, L') = \frac{1}{k}\sum_k d^2(L(x,y)| \quad |, L'(x,y))L'$$ (4)

In Eq. (4), k is the pixels' number in the image and d is the distance between the signal- the only image and the noisy image.

(C) Edge detection

One of the most significant aspects of picture pre-processing is edge detection. Only the edges of the image are used to extract geometric elements of the hand. Various methods of detecting edges include the Sobel method, Prewitt method, Roberts method, and the Canny method. In this study, Sobel edge detection was used for edge detection. Each pixel position in the image is used to compute the image's gradient.

3.2 Feature Extraction

3.2.1 Features of the Hand

Each individual hand has several features that can be used for recognition. As shown in Fig. 4, some of these features include finger length (FL), finger width (FW), finger sub-length (FSL), palm width (PW), palm length (PL), thumb length (TL), and thumb width (TW). Hand length and its contour (HL and HCL), and hand area (HA), are other features of the entire hand considered. The HL, FL, FW, and PW are frequently used traits for hand recognition and are regarded to be invariant with time and age [1]. The distance between finger lines in a finger is known as the finger sub-length (see Fig. 4).
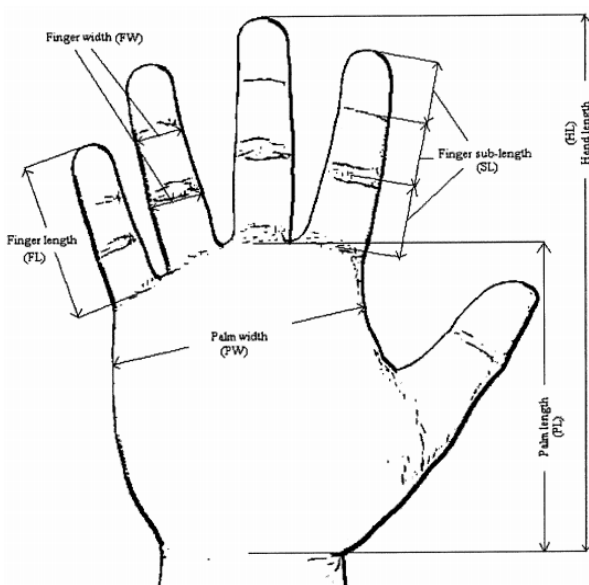
Fig. 4 Hand geometry showing some features of the hand.

3.2.2 Detection of Landmark Points

The following steps was carried out to identify the landmark points in the hand images:

1. Detection of fingertip and gap between finger tips: The point at the top of the fingertip is regarded as the fingertip point, while the lowest point of the gap between two fingers is known as the gap between finger points. The black and white image line was scanned from top to bottom. When the scan line crosses the four fingers (often five fingers) as depicted in Fig. 5(a), the scanning process stops. Then, the four cutting spots in that line are determined as shown in Fig. 5(b). By sliding the beginning points up or down along the edge, the lower gap points and the four fingertip points were discovered (see Fig. 5(c)).

2. Detection of the points of "side-points" and "palm-width-reference": The three lower gap points from Fig. 5(c), was used to estimate side points. This is done by drawing a straight line (see Fig. 5(d)) connecting the left two gap locations for the left "side-point". The intercept point between the line and the left edge can thus be designated as the "left-side" point while the intercept locations between the line and the left edge is designated as the "right-side" point. The two "palm-width-reference" points were obtained by dragging the two "side-points" down a little over the edge (around 20 pixels).

3. Detection of the four "finger-end" points: The four "finger-end" points can be calculated using the three "gap-between finger" and the two "side-point" by taking the mid-point of each pair of the gap and side points as shown in Fig. 5(e).

4. Detection of the wrist point: As shown in Fig. 5(f), the wrist is located by scanning the image from bottom to top, taking note of the white pixel width for each row. When the inside white pixel width changes rapidly (by more than 20 pixels), the scanning process stops, and the wrist is located. The wrist point is located in the middle of the white pixel line where quick changes occur (Fig. 5 (g)).

5. Detection of two "finger-line" points of each of the four fingers: The lines on the finger are referred to as "finger-lines." Because all finger-lines are horizontally oriented, Fig. 5(h) is a complete line image, while Fig. 5 (i) only shows the horizontal lines. All continuous lines no longer than 10 pixels long were searched. The black and white image is then used as a mask to remove all lines that are not within the four fingers. A mid-point is calculated for each of the remaining lines. The finger line point was obtained by averaging localized mid-points, as shown in Fig. 5(j), and then Fig. 5(k) was obtained.

6. Detection of "finger-width" reference points: For each finger, there are four "finger-width" reference points. They are placed at 1/3 and 2/3 of the finger length, which is defined as the distance between the "tip" and "end" points of the finger. The two right "finger-width" reference points were identified for each finger by using the "gap-between-finger" or "finger-tip" points (Fig. 6(a)). The two left "finger-width" reference points were then calculated by locating places on the left side with the smallest distance to the two right "finger-width" reference points as shown in Fig. 6(b).

After these operations, all the major control points on the hand features were obtained as illustrated in Fig. 6(c).
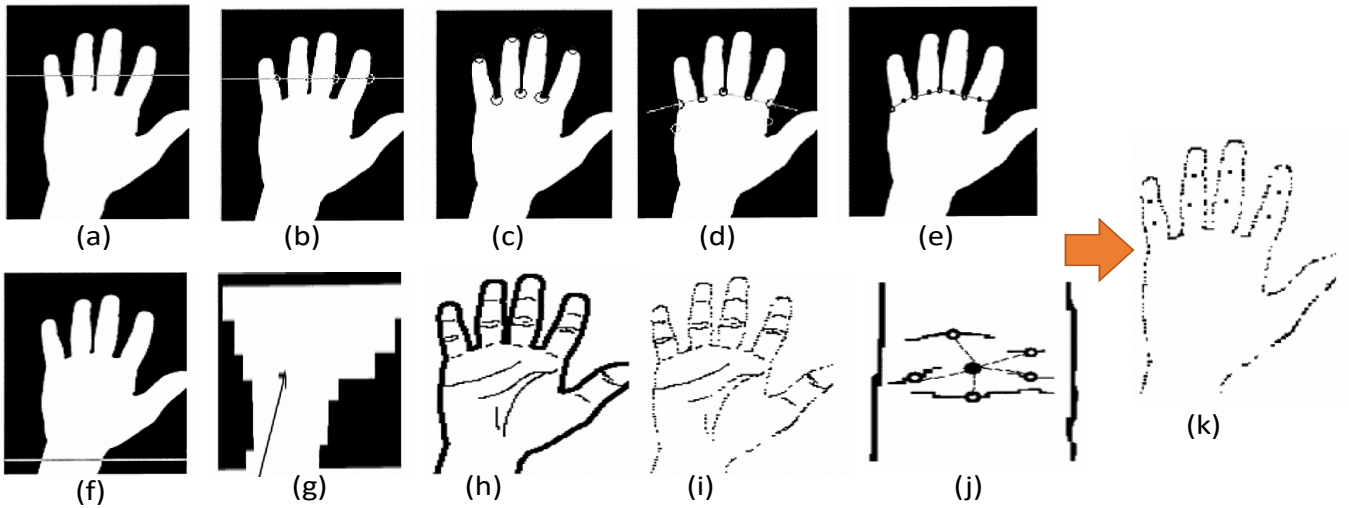
Fig. 5 Detection of landmark points (a) scan line cut the 4 fingers (b) intercepting points (c) detected fingertip and gap points (d) two side palm width reference points are predicted by using 3 gap points (e) two side palm width reference points are predicted by using 3 gap points (f) scan from bottom (g) rapid change detected (h) original detected line (i) horizontal line image (j) average of all localized points (k) all "finger-line" points.
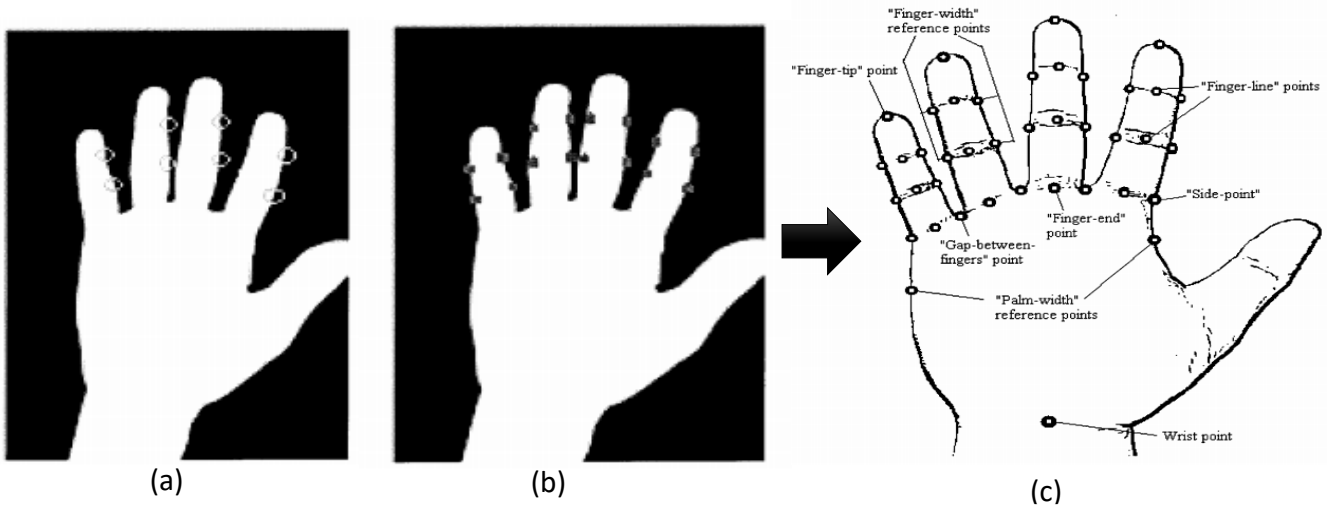
Fig. 6 Detection of "finger-width" reference points (a) right side finger width reference (b) all finger width reference (c) every control point discovered.

3.3   ANN Training and Testing

The training, validation, and testing of the data are achieved through the ANN. Fig. 7 shows the flow chart of the ANN training and testing. A back propagation neural network (BPNN) is utilized at this stage to identify features that have been removed and included in a database. The BPNN employed in this method has three layers: one input layer with 50 nodes representing 50 features, one hidden layer with 10 nodes representing one output; and one output layer with 10 nodes representing one output, as shown in Fig. 8 displays the ANN topology used for network modelling and simulation using the parameters listed in Table 2. The topology displays an overview of the neural network stimulation, the algorithm employed, the progress, and many plot options for analyzing the network's results. The data produced from the hand feature extraction measurement makes up the training data set. In the neural fitting network, the inputs used were the distances calculated for feature extraction. 70% of the parameters were used for training, while 15% each were used for both validation and testing.
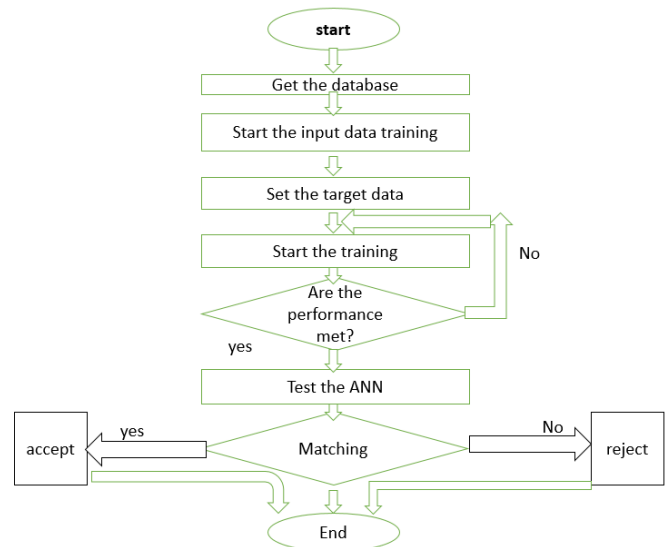
Fig. 7 Flow chat for the ANN training.
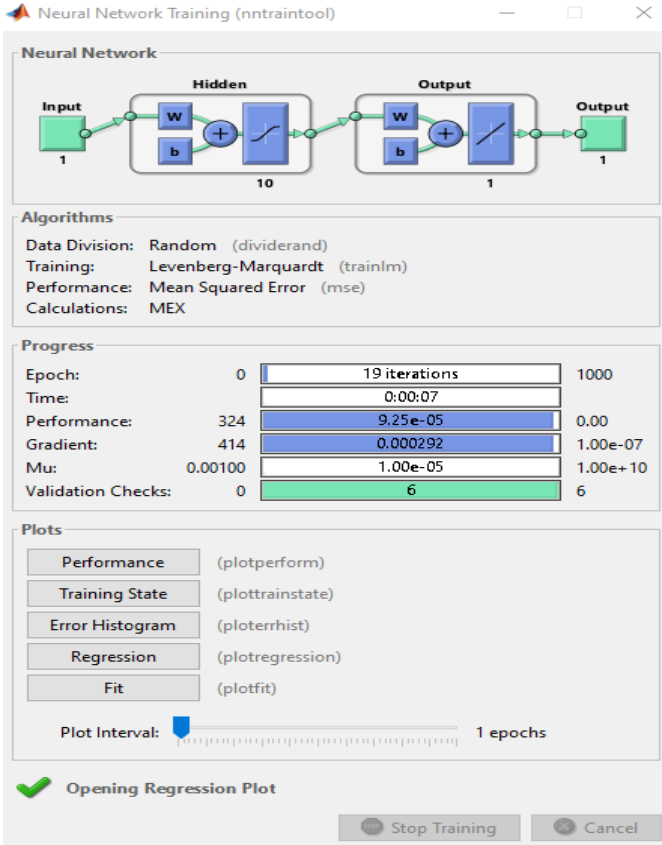
Fig. 8 The neural network architecture.

A Levenberg-Marquardt (LM) backpropagation algorithm was used during ANN training with trainlm, which is a MATLAB function that updates weight and bias values according to LM optimization.

Table 2 Parameter used for training the dataset.

Parameters	Description
Training	LM (trainlm)
Network	Feedforward BPN
Learning Function	Learngdm
Hidden Layer	01
No of neurons	19
Max. epoch	1000

3.3.1 Back-propagation Training Stage

The following steps was used during the BPNN training stage;

1. Initialization stage: All network weights and threshold levels are set to random values that are distributed uniformly within a limited range $\frac{-25}{f_i}, +\frac{25}{f_i}$, where f_i is the total number of inputs of neuron i in the network.
2. Activation stage: Apply inputs to the BPNN to activate it. If $x_1(p), x_2(p),.....,x_n(p)$ denotes the input parameters and the desired outputs is represented by $y_{d.1}(p)$, $y_{d.2}(p),.....,y_{d.n}(p)$;
   a. Actual outputs of the neurons in the hidden layer is estimated using

$$y_j(p) = sigmoid\left[\sum_{i=1}^{n} x_i(p) \times w_{ij}(p) - \theta_j\right] \quad (5)$$

where n is the number of inputs of neurons j in the hidden layer, sigmoid is the activation function.
   b. The neurons' real outputs in the hidden layer is obtained using;

$$y_k(p) = sigmoid\left[\sum_{j=1}^{n} x_{jk}(p) \times w_{jk}(p) - \theta_k\right] \quad (6)$$

3. Weight training stage: Weight in the BPNN is updated. For the output layer;
   a. The error gradient for the neurons in this layer is obtained using

$$\partial_k(p) = y_k(p) \times [1 - y_k(p)] \times e_k(p) \quad (7)$$

where $e_k(p) = y_{d.k}(p) - y_k(p)$.
   b. Evaluate the weight corrections as

$$\Delta w_{jk}(p) = \alpha. y_j(p). \partial_k(p), \quad (8)$$

   c. Weights at the output is estimated using

$$\Delta w_{jk}(p + 1) = w_{jk}(p) + \Delta w_{jk}(p). \quad (9)$$

For hidden layers;
   a. The error gradient for the neurons in this layer is obtained as;

$$\partial_j(p) = y_k(p) \times [1 - y_j(p)] \times \sum_{k=1}^{i} \partial_k(p)w_{jk}(p), \quad (10)$$

   b. The weight correction and its update at the hidden neurons are estimated using the following equations

$$\Delta w_{ij}(p) = \alpha. x_i(p). \partial_j(p) \text{ and} \quad (11)$$

$$\Delta w_{ij}(p + 1) = w_{ij}(p) + \Delta w_{ij}(p). \quad (12)$$

4. Iteration stage: Perform iterations and repeat the process until the error threshold is met.

3.4 Matching

At this stage, the features extracted in the preceding part are compared to the features of that individual already in the database. To determine if the claimant is the claimed person or not, distance functions are used. The absolute distance D_a function is employed to match the feature vector [13], [38]. This is estimated as

$$D_a = \sum_{i}^{d} |y_i - f_i| \quad (13)$$

where $f_i = h (f_1, f_2 …… f_d)$ is a d-dimensional Eigen vector of a registered user in the database, and $y_i = h (y_1,y_2 …..y_d)$ is a d-dimensional Eigen vector an unknown or the hand that is being verified (claimant). As a result, the distance between the claimant and the register user is equal to the difference between the claimer feature vector y_i and the database feature vector f_i. The system compares the result to a predetermined threshold and classifies the hand being verified after computing the distance. The hand being verified is accepted if and only if the estimated distance is less than the threshold. However, if the distance is above the threshold, the hand image is rejected.

The development and analysis were done using MATLAB software. A graphical user interface (GUI) was also developed

to facilitate easy usage of the peg-free hand geometry system. The system is validated and its performance is analyzed.

3.5 Biometric Performance Analysis

The system performance was carried out using the following terms;

3.5.1 False Rejection Rate (FFR)

The FFR occurs when a valid user is denied access because the system cannot match the current biometric data to that in the database templates. The FRR was estimated using the equation [18].

$$FRR = \frac{N_{FR}}{N_{att}} \qquad (14)$$

where NFR is the number of false rejection and N_{att} denotes the total number of attempts.

3.5.2 False Acceptance Rate (FAR)

When the system detects that the biometric data of an impostor matches the template of a legitimate user, the impostor is accepted and granted access. FAR was calculated using

$$FAR = \frac{N_{FA}}{N_{att}} \qquad (15)$$

where NFA is the number of false attempts.

3.5.3 Equal Error Rate (EER)

The EER is a measure of the point where FRR equals the FAR. It should be noted that FRR and FAR are not continuous functions, and in practice, a crossover point may not exist [38]. The ERR is a measure of a device's accuracy; the lower the ERR, the better the system. Also, the performance of the ANN used for training and classification is evaluated using the mean square error, error histogram, and regression analysis.
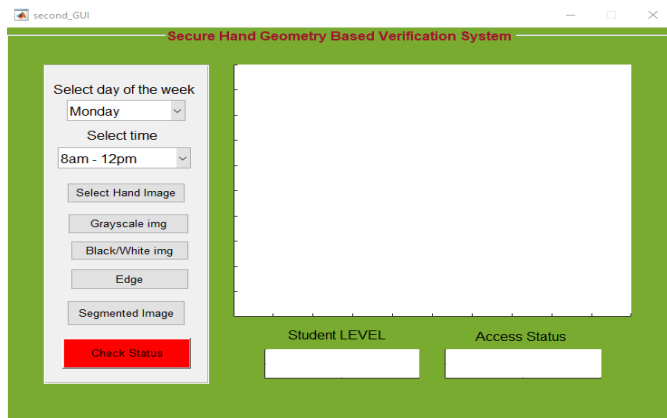
Fig. 9 The developed GUI showing several pre-processing features and access status.

4 Results and Discussions

4.1 The Developed Graphical User Interface and Implementation

As mentioned earlier, a GUI was developed to facilitate usage of the hand geometry system for access control. Also, the system was developed for use and implemented to permit or deny students' entry to a lecture hall in a tertiary institution. The developed GUI is shown in Fig. 9. As may be observed, the interface consists of two toggle buttons which are used to choose the day and time for lectures, respectively, five buttons (select hand image, grayscale image, black/white image, edge detection and segmentation) which may be used to show different pre-processing steps and a check status button which indicates the decision of the system whether to grant access or deny entry to the hall. The results produced while activating each of the buttons in Fig. 9 are illustrated in Fig. 10 to Fig. 12.
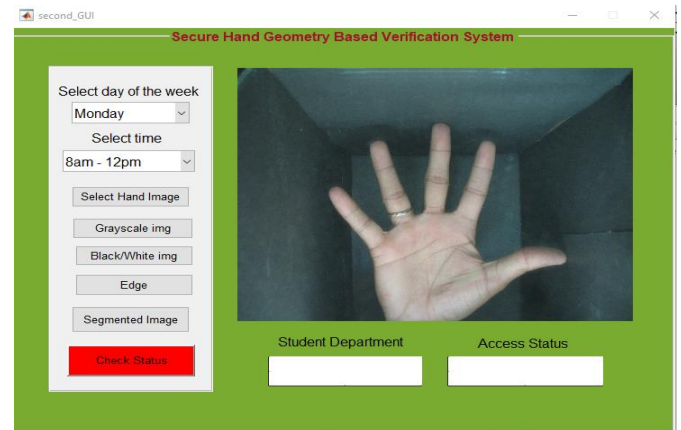
(a)
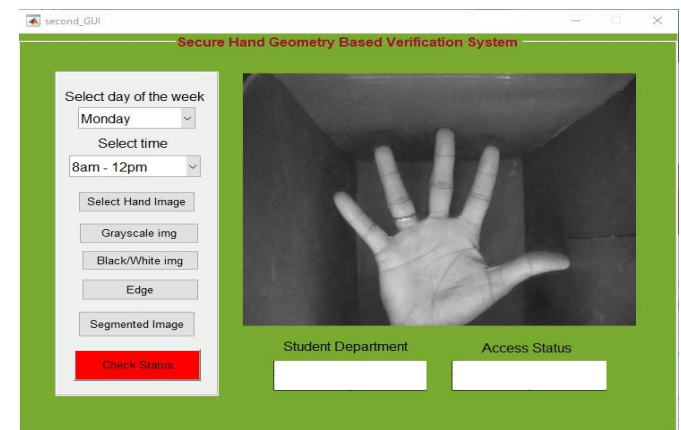
(b)

Fig. 10 The GUI showing (a) selecting the hand image (b) conversion to grayscale image.

In Fig. 10(b), the coloured image was converted to a grayscale image. The grayscale image is then converted to black and white, and the results are shown in Fig. 11(a). The next step is edge detection. In order to obtain the geometric features of the hand, the image should contain edges. This is done by using the Sobel edge detection function in the MATLAB image processing toolbox.

The result obtained after the edge detection process is shown in Fig. 11(b). The next step is the segmentation of the image, where the image is partitioned into various subgroups of pixels, which can reduce the complexity of the image and make the image easier to analyze. Fig. 12 shows the result of the image after segmentation has been performed.

4.2 Feature Validation Results

After training the dataset, the system checks and validates the hand image chosen according to the specification of the system. In this case, the system checks with respect to the class and also the timetable displayed in Table 1.
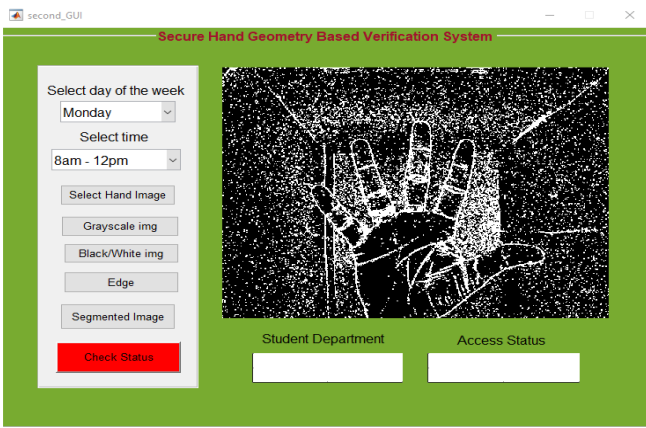
(a)
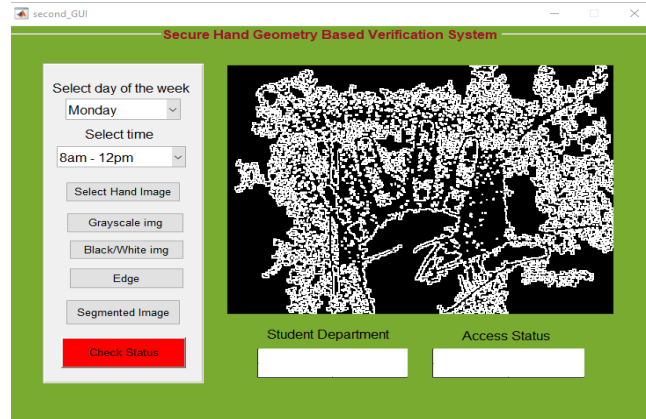
(b)

Fig. 11 The GUI showing (a) black and white conversion of the hand image (b) the image after edge detection.
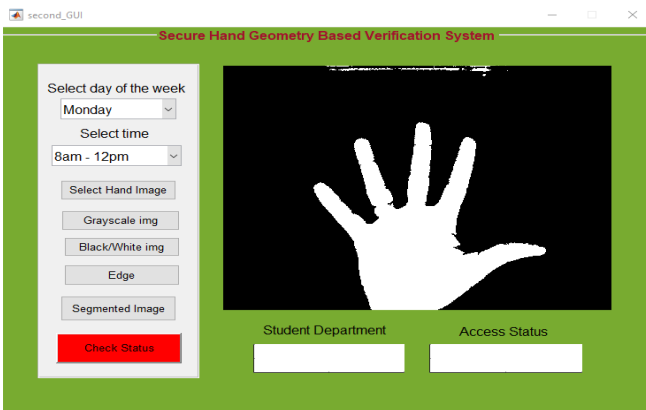
Fig. 12 The GUI showing results of the hand image after segmentation.

When an image is chosen and the system wants to validate the image, it tells if the image is accepted or declined according to the class and timetable. For example, Fig. 13(a) depicts the result of an image validation to gain access to a 300-level class for the time period 8am-12pm, whereas Fig. 13(b) depicts the result of a declined image to gain access to the same class and time because the hand image validation to the specification failed.

4.3   ANN Performance Assessment Results

Fig. 14 shows the variation of the MSE with epoch during training, validation, and testing for the LM algorithm.
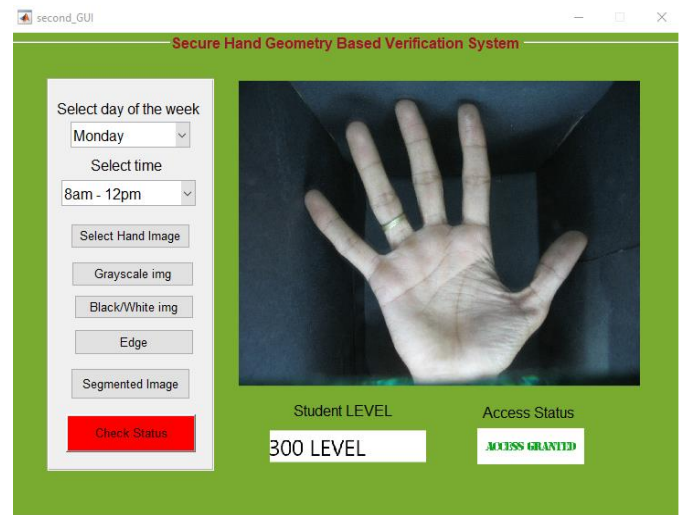
(a)
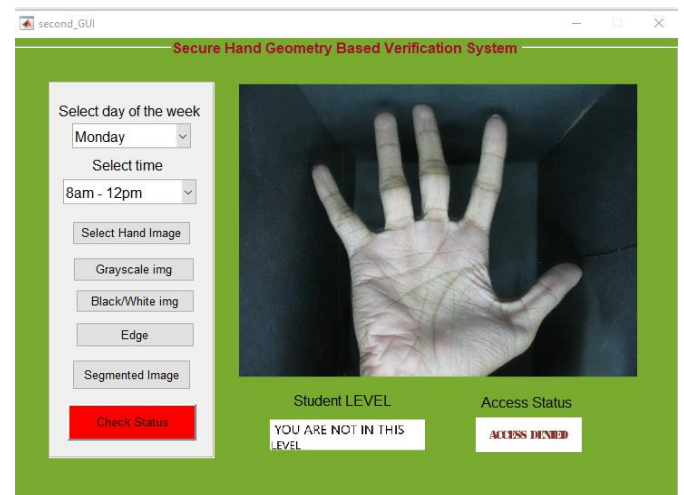
(b)

Fig. 13 GUI of the developed hand geometry system showing the access status and student level for (a) access granted (b) access denied.

As the number of epochs increases, the error starts to reduce. The error decreases sharply up to the last 6 epochs, after which it reduces gradually. If the epoch is increased beyond best performance, the validation graph tends to get more errors, which leads to overfitting of the data. During the training, the MSE is 1.25×10^{-4} at 10 iterations, with the best validation performance being 8.8383×10^{-5} at 13 epochs. The validation error was lowest at the 13th epoch, thus the training ended. It is important to state that the training is terminated after six consecutive upswings in validation error in the default configuration; thus, the best performance is selected from the epoch with the lowest validation error. After the training, the MSE becomes 9.25×10^{-5} at 19 epochs, with the best validation performance being 8.8383×10^{-5} at 13 epochs. Because the validation error was lowest at the 13th epoch, training was halted and weights and biases were used for future modelling.

The error histogram plot for the ANN is also presented as shown in Fig. 15. As may be observed, the amount of vertical bars on the graph is referred to as bins. Here, the overall error range is broken down into 20 smaller bins.

Best validation performance is 8.8383e^{-05} at epoch 13
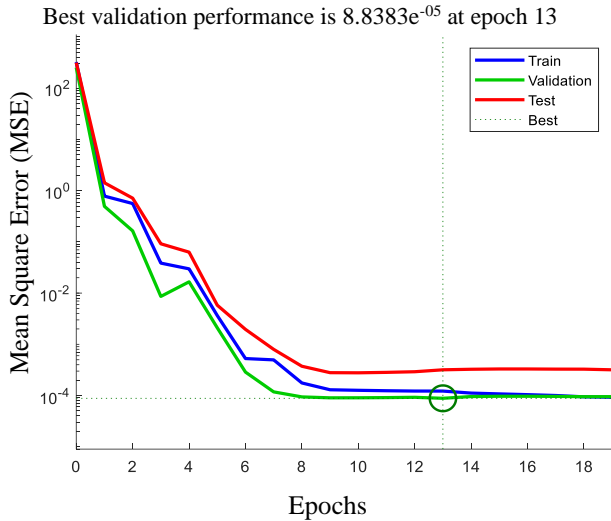
Fig. 14 Plot of the MSE against the Epochs.

The number of samples from the dataset that fall into each bin is represented on the y-axis, and the zero error line corresponds to the zero error value on the x-axis. The image dataset has an error range of around 12 samples when tested and an error range of 9.187×10^{-3} around 12 samples during validation, as shown in this graph.
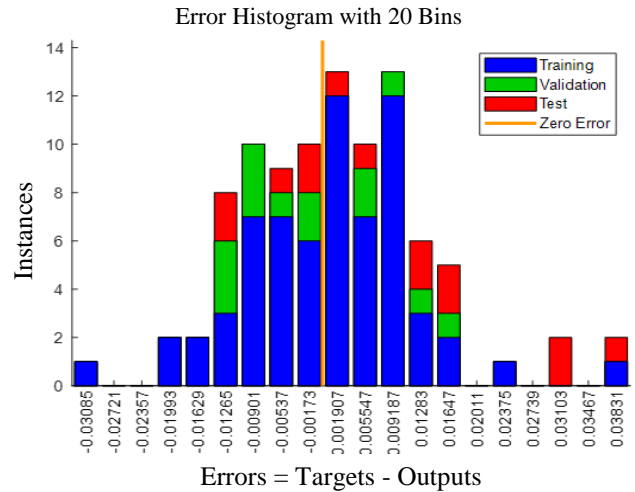
Fig. 15 The error histogram plot.

Fig. 16 shows the regression plot for the ANN. As may be observed, during training, the regression value amounts to about 0.9999. For validation, the regression value is 1, and 0.99998 for testing. When the three processes (training, testing, and validation) were considered, the regression value amount to 0.99999. This regression value indicates that the algorithm is 99.99% accurate in fitting the data.
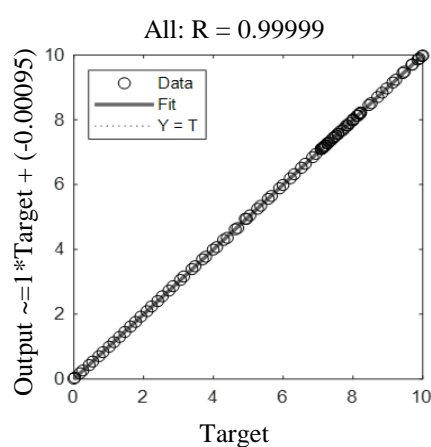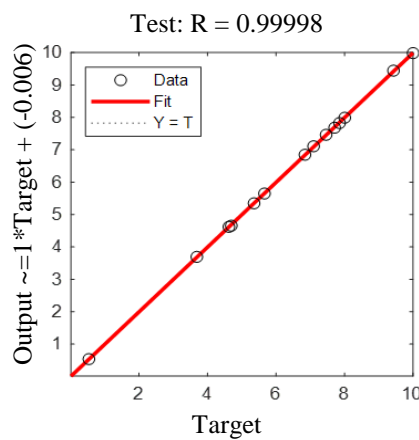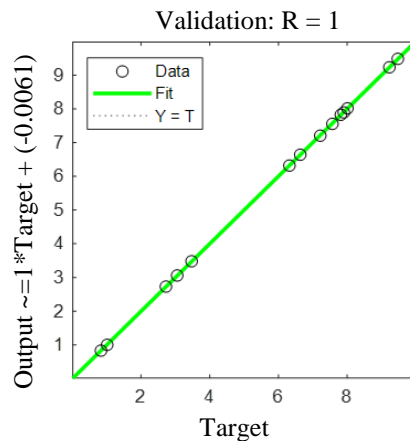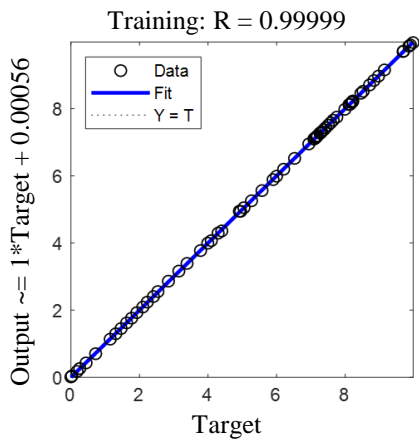
Fig. 16 Regression plot.

4.4 FAR and FRR Results

The FAR and FRR are estimated at different thresholds of the image and the results are illustrated in Fig. 17. It is observed that the FRR decreases drastically as the threshold increases up to a value of 2.5, after which it reduces slightly. Whereas the FAR increases slightly as the threshold increases.
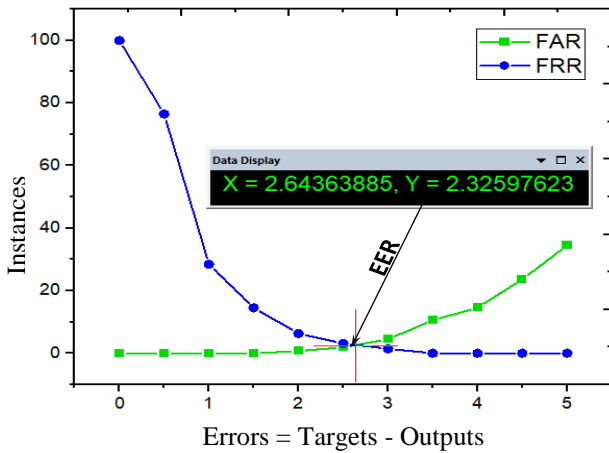
Fig. 17 Variation of the FAR and FRR with the threshold.

The system has an EER of 2.3. The arbitrary threshold proved to be good after testing with the images. There is a total of one false acceptance in every 100 tests, giving the arbitrary criterion a FAR of 0.01. In addition, 2 rejections were discovered in 100 tests, giving the FRR a value of 0.02. As may be observed in Fig. 17, it is pertinent to know that at lower threshold values, the system performs better with a relatively high FRR and a relatively low FAR.

4.5 Compared Performance Analysis

The performance of the hand geometry recognition system with related studies in the literature is presented in Table 3. The comparison was based on the size of the database, the FRR performance, FAR, EER, MSE, and regression. The results shown in Table 3 revealed that the hand geometry system presented in this paper performed better than most of the studies reported in Table 3. The FRR and FAR obtained in the proposed system are lower than those in Table 3. Aside from the studies in [35] that have a FAR of 0.0%, the proposed system has better performance than the other studies reported in Table 3. Also, the proposed system has a good regression percentage of 99.99% and a very low mean square error of 8.84×10^{-5}. Although these analyses (the regression and MSE) were investigated in other related studies presented in Table 3, In terms of the size of the database, aside from the authors in [32] that use a large database, most of the studies presented in Table 3 utilize a relatively small-to-medium database, which may not be enough to guarantee a superb performance. The database used for the current study is considered relatively large when compared to other studies in Table 3

. It is obvious from that the literature lacks a deeper analysis of the hand geometry recognition system, a gap that was filled in the current paper.

Table 3 Comparison with other similar studies

References	Technique used	Database size	FRR	FAR	MSE	Regression
[19]	Multiclass SVM	144	2.05%	0.69	na	na
[27]	Euclidean distance classifier	360	na	0.8%	na	na
[28]	Time average	470	3.4%	0.45%	na	na
[29]	Wavelet features (Nearest neighbour)	120	10.4%	11.4%	na	na
[31]	na	na	1%	0.48%	na	na
[32]	Neural net	2800	0.148%	0.357%	na	na
[30]	Geometric classifiers	714	3% (verification) 6% (identification)	<1%	na	na
[33]	Fusion of 3D and 2D hand geometries	120	10.4%	11.4%	na	na
[34]	Regression Neural Network	140	15%	15%	na	na
[35]	na	60	1.19%	0.0%	na	na
[36]	Fusion of 3D and 2D hand geometries	na	na	na	na	na
Current study	ANN	1344	0.02%	0.01%	8.84×10^{-5}	99.99%
na: Not available						

5 Conclusion and Future Work

In this paper, a peg-free hand-geometry recognition system is presented. To facilitate easy usage of the hand geometry recognition system (peg-free), a GUI was developed using MATLAB software. The developed system was validated and the overall result shows that the system can be used for biometric verification using hand geometry where the orientation and placement of the hand is not a necessity. Also, the use of an artificial neural network for the peg-free hand

geometric recognition system yielded high-performance and high-accuracy results. The system has a very low mean square error and a regression value close to 1. The results obtained also show that the system has a relatively low false acceptance rate and a relatively high false rejection rate. Although the orientation and placement of the hand does not affect the performance of the system, it is noteworthy to mention that the best result can be obtained when the hand placement does not exceed 30 degrees. Therefore, further research studies can be conducted to get an efficient result when the placement of the hand is higher than 30 degrees.

References

[1] Dutagaci, H., Sankur, B. and Yörük, E., 2008. Comparative analysis of global hand appearance-based person recognition. *Journal of Electronic Imaging, 17*(1), p.011018.

[2] Yachongka, V., Yagi, H. and Oohama, Y., 2021. Biometric identification systems with noisy enrollment for gaussian sources and channels. *Entropy, 23*(8), p.1049.

[3] Wang, M., Hu, J. and Abbass, H.A., 2020. BrainPrint: EEG biometric identification based on analyzing brain connectivity graphs. *Pattern Recognition, 105*, p.107381.

[4] Kortli, Y., Jridi, M., Al Falou, A. and Atri, M., 2020. Face recognition systems: A survey. *Sensors, 20*(2), p.342.

[5] Sepas-Moghaddam, A., Pereira, F.M. and Correia, P.L., 2020. Face recognition: a novel multi-level taxonomy based survey. *IET Biometrics, 9*(2), pp.58-67.

[6] del Rio, J.S., Moctezuma, D., Conde, C., de Diego, I.M. and Cabello, E., 2016. Automated border control e-gates and facial recognition systems. *Computers & Security, 62*, pp.49-72.

[7] De Marsico, M., Nappi, M., Riccio, D. and Tortora, G., 2013. Entropy-based template analysis in face biometric identification systems. *Signal, Image and Video Processing, 7*(3), pp.493-505.

[8] Nguyen, K., Fookes, C., Jillela, R., Sridharan, S. and Ross, A., 2017. Long range iris recognition: A survey. *Pattern Recognition, 72*, pp.123-143.

[9] Salve, S.S. and Narote, S.P. 2016. Iris recognition using SVM and ANN. In Proceedings of the *IEEE International Conference on Wireless Communications, Signal Processing and Networking*, 23-25 March, Chennai, India. pp. 474-478.

[10] Hezil, H., Djemili, R. and Bourouba, H., 2018. Signature recognition using binary features and KNN. *International Journal of Biometrics, 10*(1), pp.1-15.

[11] Piciucco, E., Maiorana, E. and Campisi, P., 2018. Palm vein recognition using a high dynamic range approach. *IET Biometrics, 7*(5), pp.439-446.

[12] Abed, M.H., 2017. Wrist and Palm Vein pattern recognition using Gabor filter. *Journal of AL-Qadisiyah for Computer Science and Mathematics, 9*(1), pp.49-60.

[13] Funada, J.I., Ohta, N., Mizoguchi, M., Temma, T., Nakanishi, K., Murai, A., Sugiuchi, T., Wakabayashi, T.

and Yamada, Y., 1998, August. Feature extraction method for palmprint considering elimination of creases. In Proceedings. *Fourteenth International Conference on Pattern Recognition* (Cat. No. 98EX170) (Vol. 2, pp. 1849-1854). IEEE.

[14] Sancen-Plaza, A., Contreras-Medina, L.M., Barranco-Gutiérrez, A.I., Villaseñor-Mora, C., Martínez-Nolasco, J.J. and Padilla-Medina, J.A., 2020. Facial recognition for drunk people using thermal imaging. *Mathematical Problems in Engineering, 2020*, Article ID 1024173.

[15] Abozaid, A., Haggag, A., Kasban, H. and Eltokhy, M., 2019. Multimodal biometric scheme for human authentication technique based on voice and face recognition fusion. *Multimedia Tools and Applications, 78*(12), pp.16345-16361.

[16] Yoruk, E., Konukoglu, E., Sankur, B. and Darbon, J., 2006. Shape-based hand recognition. *IEEE Transactions on Image Processing, 15*(7), pp.1803-1815.

[17] Mostayed, A., Kabir, M.E., Khan, S.Z. and Mazumder, M.M.G., 2009, December. Biometric authentication from low resolution hand images using radon transform. In 2009 *12th International Conference on Computers and Information Technology* (pp. 587-592). IEEE.

[18] Hussein, N.M.S., Hammed, S.M., and Ergen, B. 2017. Biometric identification system based on hand geometry. *International Journal of Innovative Research in Science, 6*(3), pp. 3159–3166.

[19] Angadi, S. and Hatture, S., 2018. Hand geometry based user identification using minimal edge connected hand image graph. *IET Computer Vision, 12*(5), pp.744-752.

[20] Taher, M.M. and George, L.E., 2022a. A digital signature system based on hand geometry-Survey. *Wasit Journal of Computer and Mathematic Science, 1*(1), pp. 1-14.

[21] Taher, M.M. and George, L.E., 2022. A digital signature system based on hand geometry. *Journal of Algebraic Statistics, 13*(3), pp.4538-4556.

[22] Mohammed, H.H., Baker, S.A. and Nori, A.S., 2021, February. Biometric identity Authentication System Using Hand Geometry Measurements. In *Journal of Physics: Conference Series* (Vol. 1804, No. 1, p. 012144). IOP Publishing.

[23] Dvořák, M., Drahanský, M. and Abdulla, W.H., 2021. On the fly biometric identification system using hand-geometry. *IET Biometrics, 10*(3), pp.315-325.

[24] Ghanbari, S., Ashtyani, Z.P. and Masouleh, M.T., 2022, May. User Identification Based on Hand Geometrical Biometrics Using Media-Pipe. In 2022 30th *International Conference on Electrical Engineering (ICEE)* (pp. 373-378). IEEE.

[25] Fang, L., Liang, N., Kang, W., Wang, Z. and Feng, D.D., 2020. Real-time hand posture recognition using hand geometric features and fisher vector. *Signal Processing: Image Communication, 82*, p.115729.

[26] Masood, D. and Qi, J., 2022. 3D Localization of Hand Acupoints Using Hand Geometry and Landmark Points Based on RGB-D CNN Fusion. *Annals of Biomedical Engineering*, pp.1-13.

[27] Boreki, G. and Zimmer, A., 2005, October. Hand geometry: a new approach for feature extraction. In *Fourth IEEE Workshop on Automatic Identification Advanced Technologies (AutoID'05)* (pp. 149-154). IEEE.

[28] Adán, M., Adán, A., Vázquez, A.S. and Torres, R., 2008. Biometric verification/identification based on hands natural layout. *Image and Vision Computing, 26*(4), pp.451-465.

[29] Villegas, O.O.V., Domínguez, H.D.J.O., Sánchez, V.G.C., Maynez, L.O. and Orozco, H.M., 2006. Biometric human identification of hand geometry features using discrete wavelet transform. *Discrete Wavelet Transforms–Biomedical Applications*, pp.251-266.

[30] Bulatov, Y., Jambawalikar, S., Kumar, P. and Sethia, S., 2004, July. Hand recognition using geometric classifiers. In *International Conference on Biometric Authentication* (pp. 753-759). Springer, Berlin, Heidelberg.

[31] Dhole, S.A. and Patil, V.H., 2012. Person identification using peg free hand geometry measurement. *International Journal of Engineering Science and Technology, 4*(6), pp.2943-2949.

[32] Martinez, F., Orrite, C. and Herrero, E., 2005, June. Biometric hand recognition using neural networks. In *International Work-Conference on Artificial Neural Networks (pp. 1164-1171).* Springer, Berlin, Heidelberg.

[33] Kanhangad, V., Kumar, A. and Zhang, D., 2009, June. Combining 2D and 3D hand geometry features for biometric verification. In 2009 IEEE Computer Society *Conference on Computer Vision and Pattern Recognition Workshops* (pp. 39-44). IEEE.

[34] Polat, Ö. and Yıldırım, T., 2008. Hand geometry identification without feature extraction by general regression neural network. *Expert systems with* Applications, 34(2), pp.845-849.

[35] Klonowski, M., Plata, M. and Syga, P., 2018. User authorization based on hand geometry without special equipment. *Pattern Recognition, 73*, pp.189-201.

[36] Iula, A., 2021. Biometric recognition through 3D ultrasound hand geometry. *Ultrasonics, 111*, p.106326.

[37] Iula, A. and Micucci, M., 2022. Multimodal Biometric Recognition Based on 3D Ultrasound Palmprint-Hand Geometry Fusion. *IEEE Access, 10*, pp.7914-7925.

[38] Bača, M., Grd, P. and Fotak, T., 2012. Basic principles and trends in hand geometry and hand shape biometrics. *New Trends and Developments in Biometrics*, pp.77-99.

[39] Damousis, I.G. and Argyropoulos, S., 2012. Four machine learning algorithms for biometrics fusion: A comparative study. *Applied Computational Intelligence and Soft Computing*, 2012.

Investigation on Circular Array of Turbulent Impinging Round Jets at Confined Case: A CFD Study

Sudipta Debnath[1],*, Md. Tanvir Khan[2], Zahir Uddin Ahmed[1]

[1]Department of Mechanical Engineering, Khulna University of Engineering & Technology, Khulna – 9203, Bangladesh.
[2]Department of Mechanical and System Engineering, Okayama University, Okayama – 700-8530, Japan

ABSTRACT

Jet impingement has immense applications in industrial cooling, such as glass tempering, turbine blades, electrical equipment, etc. The interplay in-between several jet arrangements and the effect of swirl intensity require enormous study to achieve steady heat transfer. This paper numerically investigates an inline array of 25 circular confined swirling air jets impinging vertically on a flat surface. In this regard, three-dimensional simulations are executed using the finite volume method for a number of control parameters, such as Reynolds number (Re = 11600, 24600, and 35000), impinging distance (H/D = 0.25, 0.5, 1), swirl number (S = 0.3 and 0.75) and jet-to-jet separation distance (Z/D = 2.5), where, D is the nozzle diameter. Impinging pressure distribution, flow velocity, surface Nusselt number, and Reynolds stresses are investigated for different operating conditions. The results reveal that both the wall pressure and surface Nusselt number are comparatively uniform in the case of high swirl flow. Moreover, distinct heat transfer behavior is observed from the unconfined condition for high swirl flow in which the heat transfer is constant after a certain radial distance. The Reynolds normal stress adjacent to the nozzle exit is more rigorous than the downstream regions while Reynolds shear stress varies unpredictably along the radial direction. In addition, an estimated 102 % enhancement in average Nusselt number is observed for high swirl flow, at a Reynolds number increment from 11600 to 35000. This enhancement is evident by 23 % in terms of thermal performance factor. Besides, the average Nusselt number and thermal performance factor augmented by 19 % and 8 %, respectively, for an increased swirl intensity at low a Reynolds number (Re = 11600).

Keywords: Thermal Performance Factor, Pressure Coefficient, Swirl, Reynolds Stress, CFD.

1 Introduction

Jet impingement is a common method of heating or cooling solid surfaces. The heat transfer rate by the impinging jet is usually higher than the other conventional methods. Because the flow of fluid in the form of a jet impingement rapidly increases its momentum. In turbulent flow, the molecules in the flowing fluid act in a random manner. Molecules in a flowing fluid transfer momentum and energy from one place to another by mixing fluid particles often called vortex mixing. Usually, the heat transfer rate in turbulent flow is high due to rising and random mixing. Therefore, the most practical use of jet impact is in industries where heat transfer requirements are greater than the capacity of conventional heating and cooling techniques. Industrial jet impingement includes drying of paper, textiles, and veneer, tempering of glass, annealing of metals and cooling of gas turbine blades, electronic components and drying of films in the film industry, application of steam to the cylindrical surfaces of the combustion chamber [1]-[5].

Martin [6] measured average mass transfer under multiple confined slot jets. In his study, the outflow was reserved to exit only in the traverse direction through the open sides at the ends of the slot nozzles and the transport rate at the impingement plate was highly nonuniform in the direction of the nozzle length. Colucci, et al. [7] implemented a thermochromatic liquid-crystal technique and examined the effects of hyperbolic nozzle geometry on the local heat-transfer coefficients for confined impinging air jets. They reckoned that the local heat-transfer coefficients for confined jets are more sensitive to Reynolds number and nozzle-to-plate spacing than those for unconfined

jets. Saad, et al. [8] investigated multiple confined impinging slot jets without crossflow effects and observed that the heat-transfer data acquired for unconfined jets cannot be employed reliably in the design of confined jets. Huber, et al. [9] studied convective heat transfer to a confined impinging array of air jets with spent air exits with the implementation of bandpass filters and an electronic digitizer board. Their results have shown that the inclusion of spent air exits increased the convective heat transfer coefficient and changed the location of the optimal separation length.

Markal [10] experimentally investigated heat transfer characteristics and wall pressure distribution of swirling coaxial confined turbulent impinging air jets at multiple nozzle-to-plate distances and flow rates for a constant total flow rate. He observed that the flowrate ratio improves the uniformity of heat transfer through the impingement surface and works better for lower impinging distance. Also in terms of pressure distribution, there are subatmospheric regions near the impact plate. He further investigated the effect of multiple total flow rates on the thermal management ability of swirling coaxial confined impinging air jets and found that both heat transfer rate and radial uniformity are improved by increasing total flow rate [11]. Habib, et al. [12] studied velocity characteristics of both non-swirl and swirl confined coaxial jets. Their results show, with swirl, the area near the recirculation of the center line and between one and three diameters of the furnace below the exit plane. Thus, as the number of swirls increases from zero, this chance of recirculation increases and is finally met. Memar, et al. [13] studied convective heat transfer data from a confining tube to coaxial, counter-swirled jets and observed that peak Nusselt

number was shifted upstream with the increase of inner jet swirl strength. Petera, et al. [14] studied both experimentally and numerically heat transfer measurements of a confined impinging jet with a tangential velocity component. They found that the addition of the tangential velocity component significantly influences the velocity field and the intensity of heat transfer in the stagnant region compared to the classical characteristics of the impinging jet. Shuja, et al. [15] investigated confined swirling jet impingement onto an adiabatic wall and found that with the increase of swirl velocity, the jet axis tilts towards the radial direction.

In order to improve convection heat transfer and minimize defects, a plethora of research has been performed to determine the effect of different parameters on multiple jet impingement flow dynamics and heat transfer. Chouaieb et al. [16] investigated the effect of a swirl generator on the mixing process using numerical simulation and found that the position of the swirl generator had a clear effect on the mixing process. Liu et al. [17] predicted the swirl length of different vortex patterns by studying the swirling flow of gas and fluid caused by fan-type vortexing in a vertical duct. The swirl length of the swirling gas column and the swirling intermittent flow increases as the surface velocity of the liquid increases or as the surface velocity of the gas decreases. Yan et al. [18] described a numerical method for investigating the uniform structure and components of turbulence associated with vortex-vortex interactions. He found that under medium and high swirl intensities, the turbulence intensity was enhanced and weakened, respectively, from the single swirling jet level, and augmented and depressed, respectively, by enlarging the jet-to-jet spacing. Fenot et al. [19] studied the flow field of the swirling impinging jets with eight channels for Re = 23,000–33,000. He believed that the internal shear layer caused the mainstream to accelerate, and vortices formed under the mainstream increased Nusselt number by 50%. Ahmed et al. [20], [21] studied the influence of inflow profile and swirl intensity on the development of turbulent impinging jets. Compared to the non-swirling jet, the turbulence kinetic energy and shear stress of the wall are significantly reduced when the weak swirling flow enters the impinging jet. Wu et al. [22] found that the pressure distribution in the four composite cooling structures was very different from swirl cooling and impingement cooling. In addition, the nozzle-nozzle mass flow ratio distribution changes with changing nozzle position, which affects flow and heat transfer characteristics. Debnath et al. [23]-[25] investigated the average flow and pressure characteristics of both swirling and non-swirling jet arrays. The results show that the swirling jet backflow intensity is greater than the non-swirling jet and provides the maximum pressure coefficient at the stagnation point of each jet. Wannassi et al. [26] studied the details of flow and the complex flow structure of a staggered combination of straight and swirling jets. They believe that the vortex rapidly disappears in the circumferential direction below the nozzle outlet, which results in an insufficient axial impulse.

Hollworth et al. [27] investigated the heat transfer field of jet impact cooling with emission holes on the target surface. They compared their results in cases without outlets and found that the nozzle field with outlets had a 20-30% higher heat transfer rate. Zhang et al. [28] compared the cooling performance of hybrid impingement cooling dend effusion cooling of a multi-swirler combustor and concluded that the hybrid impingement cooling method was very effective. Wu et al. [29] investigated an array jet impingement cooling for a simulated chip using an additively manufactured manifold design that encloses the chip

with working fluid. They created a series of extraction holes between adjacent nozzle holes to prevent cross-flow and nozzle interference between adjacent nozzles in their design. In short, extracting spent flow improves the heat transfer performance of the jet cooling field. Caliskan and Baskaya [30] investigated heat transfer in an inline jet array on smooth and rib-roughened surfaces. Through their analysis, they found an increase in the heat transfer coefficient over the surface from 4% to 26% when compared with a flat plate. Chauhan and Thakur [31] studied the heat transfer and friction factor correlations for impinging jets and observed that, the streamwise and spanwise jet-to-jet spacing enhanced the heat transfer rates.

Hatami et al. [32] performed a two-dimensional (2D) computational fluid dynamics (CFD) simulation of air-jet using two different turbulence models and found that heat transfer could be improved by almost 30% in an unconfined test case compared to a confined one. A large impact of dimensionless length was also observed in achieving maximum heat transfer. C. Wang et al. [33] experimentally investigated the air jet with uniform constant heat flux boundary condition and found that air velocity near the impact area was an important factor in improving heat transfer. Katti et al. [34] conducted experimental measurements of single free jet heat transfer and Jeffers et al. [35] examined the stagnation zone with a single confined and submerged impinging jet. Both of them noticed that stagnant pressure could migrate to the exit of the nozzle and change the nozzle outlet velocity profile in the proximity of the nozzle exit. Ekkad and Han [36] demonstrated transient liquid crystal thermography techniques and other gas turbine cooling technologies. Their work reveals important details of the two-dimensional heat transfer distribution. Ichikawa et al. [37] investigated the flow behavior of a series of circular jets by varying the nozzle to plate distance and nozzle to nozzle distance and found that heat transfer performance was increased by a configuration that included nozzle to plate distance 2 and nozzle to nozzle distance 4. Buzzard et al. [38] and Ligrani et al. [39] studied the impact of a rough surface in the jet impingement field and found an increase in surface heat transfer and surface Nusselt number for both laminar and turbulent flow.

Although unconfined impinging jets are widely available in the literature, possibly due to their huge applicability to industrial applications and uncomplicated correlation with experimentations, in numerous functional applications heat transfer operations are applied in a confined atmosphere. Nevertheless, a few number of research has been conducted on confined impinging jets, which are often limited to non-swirl flow [35], [40]–[42]. The results show significantly different behavior of flow and heat transfer compared to their unconfined complements. Research on swirling impinging jets with flow confinements is poor in the literature. Thus, this paper will investigate the basic thermo-fluidic behavior of multiple swirling impinging jets due to the flow confinement at very small impingement distances (H/D = 0.25, 0.5, 1) for three different Reynolds numbers equal to 11,600, 24600, and 35000, at a jet-to-jet spacing Z/D = 2.5. The degree of swirl intensity is varied from medium to the highest (S = 0.3 and 0.75).

2 Methodology

A multiple swirling air jet impingement system consisting of twenty-five circular jets and a flat round surface is considered in this study. The jets emanate from an axial-plus-tangential aerodynamic swirl nozzle of diameter 40 mm in which a seamless transition from no swirl to high swirl flow can be

achieved for the identical mass flow rate. The detailed dimension of this nozzle is available in Islam et al. [43] and Khan et al. [44], [45], hence is not repeated here for brevity. The nozzles are organized in an inline arrangement and evenly distributed into three concentric circles around a central nozzle with 8 nozzles in each circle. Due to the symmetrical nature of the problem, only a quarter of the full domain was considered for the simulation to save computational costs. The physical arrangement of the nozzle array along with the coordinate setup of the computational domain and a representative schematic diagram of the swirling jet flow structure is illustrated in Fig. 1. Such a physical system is applicable to the glass tempering process in which multiple jets are used for the rapid cooling of the tempered glass after numerous heat treatment operations.
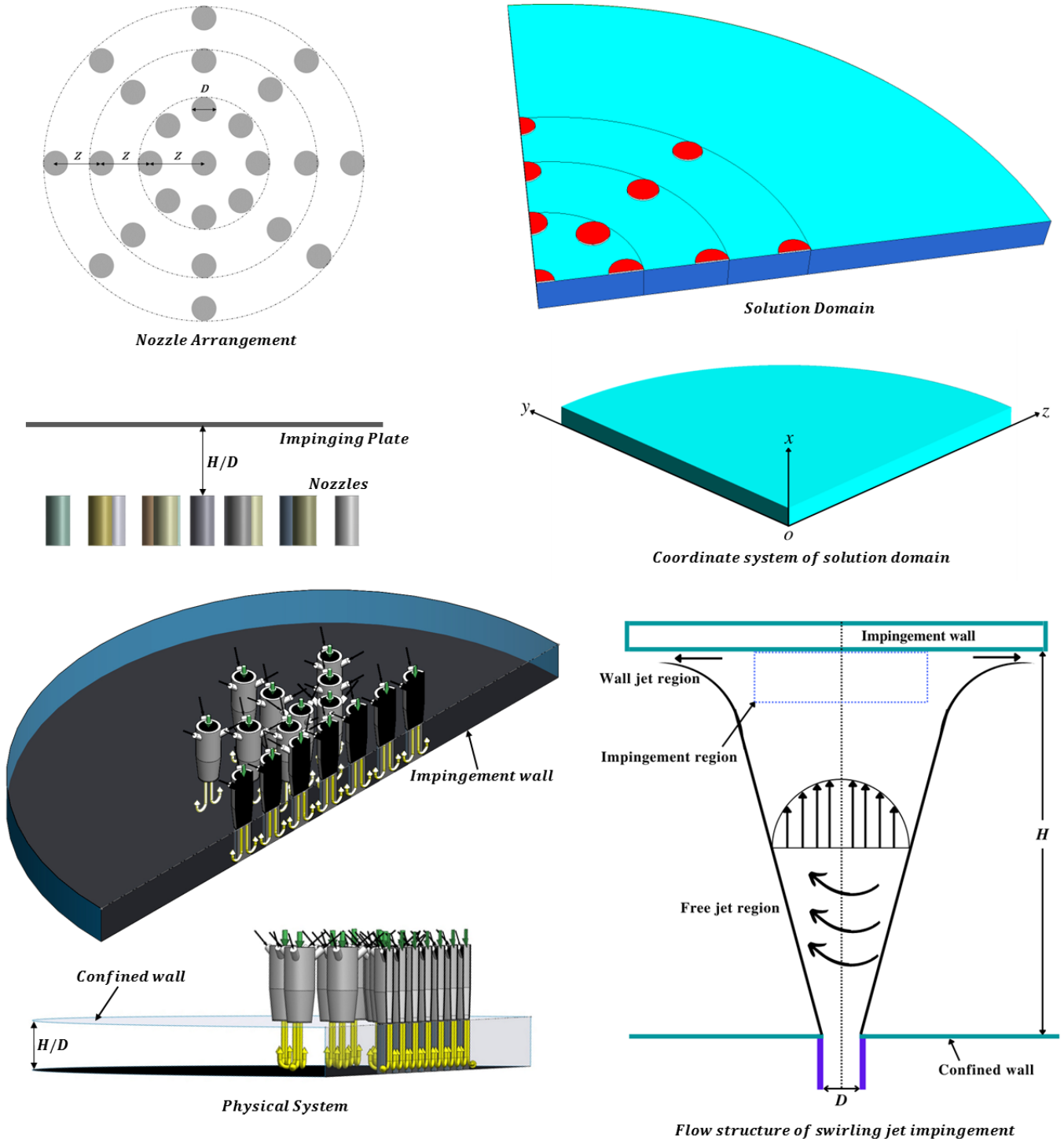
Fig. 1 A schematic view of the solution domain, the detailed of nozzles and coordinates, circular orientations of the inline nozzle arrangement, detailed illustrations of a physical system, and flow composition of the jet.

The governing equations to resolve the above $3D$ problem are the continuity equation, momentum equation, and energy equation. Turbulent flow is assumed to be resolved by the RANS approach. The governing equations in the compact form are:

$$\frac{\partial(\rho u\phi)}{\partial x}+\frac{\partial(\rho v\phi)}{\partial y}+\frac{\partial(\rho w\phi)}{\partial z}=\frac{\partial}{\partial x}\left(\Gamma_\phi\frac{\partial\phi}{\partial x}\right)+\frac{\partial}{\partial y}\left(\Gamma_\phi\frac{\partial\phi}{\partial y}\right)+\frac{\partial}{\partial z}\left(\Gamma_\phi\frac{\partial\phi}{\partial z}\right)+S_\phi \qquad (1)$$

where ϕ, Γ_ϕ and S_ϕ represent the generalized variables, effective transport coefficients, and source terms, respectively. The detailed expressions for each of the governing equations are available in [20]. The turbulence closure terms $\overline{u'_i u'_j}$ and $u'_i T$ in Eq. (1) are expressed in indicial notations as:

$$\overline{u'_i u'_j} = 2/3k\delta_{ij} - \mu_t\left(\frac{\partial u_i}{\partial x_j}+\frac{\partial u_j}{\partial x_i}\right) \qquad (2)$$

$$\overline{u'_i T'} = -\Gamma_T\frac{\partial T}{\partial x_j} \qquad (3)$$

where, μ_t is a function of k and ε or ω, which are determined via two other transport equations. The pressure velocity coupling was solved utilizing the coupled solver with Green-Gauss node-based gradient discretization. PRESTO is used for pressure discretization. Second-order upwind scheme for convective terms and second-order accurate (central difference) for diffusion terms of governing equations are applied. Residuals of each variable were set to 10^{-06}
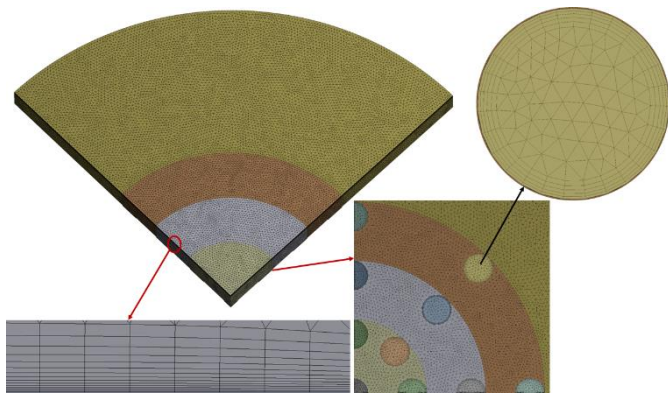
Fig. 2 Solution domain with detailed mesh in different sections.

A typical mesh for the current setup with an enlarged view of inflation layers, near the axis and inlet is shown in Fig. 2. Unstructured tetrahedral mesh with 15 prismatic layers near the surface and a growth rate of 1.2 is used to better resolve the wall characteristics. A relatively coarse mesh is created at the outer and upper boundaries of the area where variable flow is expected to be lower. A grid independence test was performed with five different numbers of nodes, namely 162k, 183k, 236k, 253k, and 293k. In this regard, the area-averaged Nusselt number is determined for circumferential area 6D of the plate for each mesh and the result of the grid independence study is presented in Table 1. It is observed that when the number of nodes is more than 236k, the variation of the area-averaged Nusselt number is less than 1%. To precisely acquire the numerical data as well as to minimize the computational cost, finally, 253k nodes were selected to execute the analysis. To accurately resolve the near-wall characteristics, the value of y+ is ensured less than unity for all cases almost in the whole simulation domain.

Table 1 Mesh independency test.

Mesh	Grid1	Grid2	Grid3	Grid4	Grid5
Elements	344805	461146	773292	842257	991763
Nodes	162830	183807	236374	253712	293480
$\overline{Nu}_{6D}$	120.38	120.71	121.38	122.14	122.16
y^+	1.29	1.22	1.06	0.98	0.88

Fig. 3 presents the applied boundary conditions on different locations of the solution domain. Boundary conditions in the simulation include the velocity of the inlet from each nozzle outlet, the non-slip and uniform state of the wall's heat flow, the atmospheric pressure on the inlet and outlet surfaces, and the adiabatic condition on the confined surface. Input conditions of different flow conditions (mean and turbulence) were obtained from the study by Ahmed [46]. Data profiles are set in all nozzles as input boundary conditions. The boundary symmetry state is applied to two side surfaces for non-swirling jets and periodic boundary conditions for swirling jets.
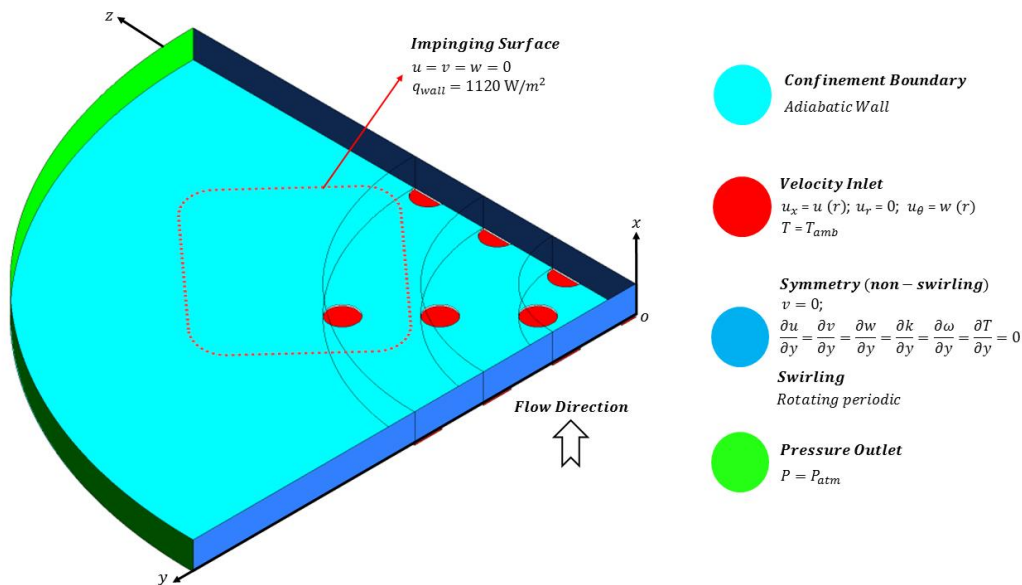
Fig. 3 Computational domain with detailed boundary conditions.

Lastly, Fig. 4 represents the numerical predictions of pressure coefficient (C_p) and surface heat transfer coefficient (h) at impinging plate along the radial line in the horizontal direction for single nozzle medium swirl ($S = 0.3$) flow at $Re = 24600$ and $H = 1D$ using three different turbulence models (SST k-ω, Transition SST and Realizable k-ε) and they are compared with the experimental data [46]. In general, the numerical projections appropriately conform to the experimental data. However, in terms of surface heat transfer coefficient, slight variations among the numerical results and experimental data are visible which might be due to the differences in nozzle diameters, particular inlet conditions, and impinging distances. Furthermore, it is observed that SST k-ω is found to be in better agreement with the experimental data among all turbulence models. As such, the current research has considered the SST k-ω turbulence model for the computational analysis using a commercial software package ANSYS Fluent v17.
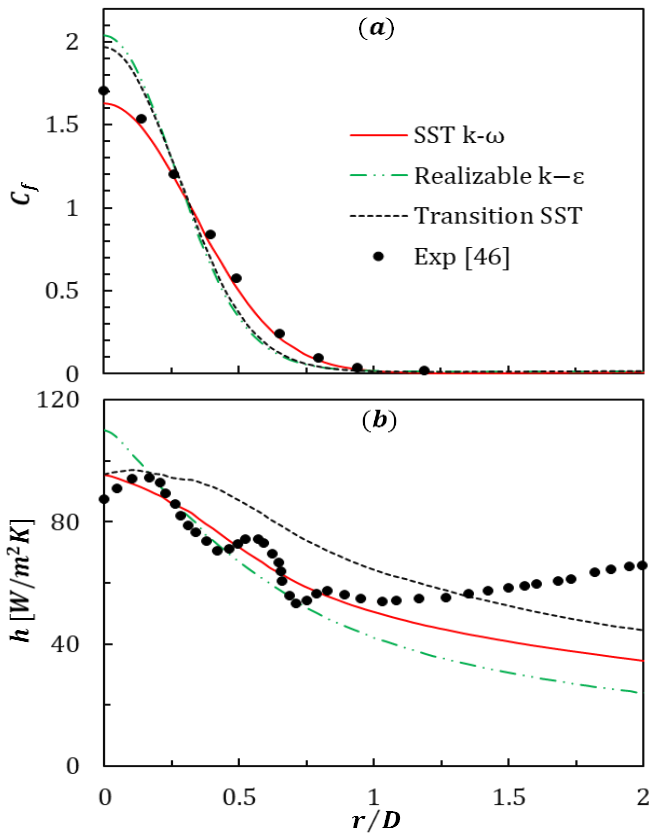
Fig. 4 Comparisons of (a) pressure coefficient (C_p) and (b) heat transfer coefficient (H) at impinging plate along the radial line in the horizontal direction for single nozzle medium swirl flow ($S = 0.3$) at $Re = 24600$ and $H = 1D$ using different turbulence models.

3   Data Reduction

$$\overline{Nu} = \frac{1}{A}\int Nu\, dA \qquad (4)$$

$$\eta = \frac{\overline{Nu}\big/\overline{Nu_o}}{f\big/f_o} \qquad (5)$$

$$\overline{Nu} = 0.408 Re^{0.583}\left(\frac{H}{D}\right)^{-0.35} S^{0.18} \ \textit{[When S = 0.3 \& 0.75]} \qquad (6)$$

4   Results and Discussion

For the analysis of the coefficient of pressure C_p, data are taken at five planes ($x/D = 0.2$, 0.4, 0.6, 0.8, and 0.95) immediately after the nozzle exit close to the impingement surface. The results are shown in Fig. 5 for both medium and higher swirling flows when $H = 1D$ and $Re = 24600$. The results for the medium-swirl flow show that the pressure adjacent to the nozzle exit is the lowest and gradually increases towards the impact plate. The results also show that the pressure is highest in areas of stagnation, where the flow impinges on the plate and then decreases radially and circumferentially. For $S = 0.75$, the static pressure in the nozzles gradually increases towards the impingement plate, similar to the medium-swirling jets. The pressure is comparatively more uniformly distributed across the impact plate in a higher swirling flow rather than a medium swirl.
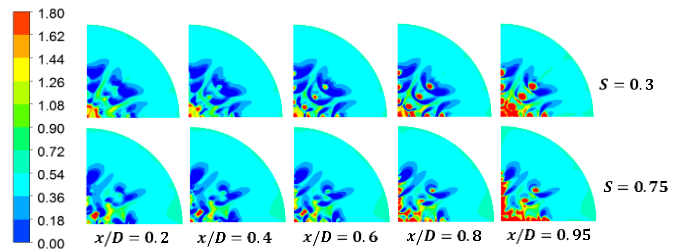
Fig. 5 Contours of pressure coefficient C_p at different axial distances of jets when $S = 0.3$ and 0.75 at $H/D = 1$ and $Re = 24600$.

Fig. 6 shows the velocity contours for $S = 0.3$ and 0.75 at different cross-sections in the axial direction for $Re = 11600$ and 35000. It can be seen from the figure that the jet velocity is maximum at the vicinity of the nozzle exit and it gradually decreases towards the impingement surface. The decreasing tendency for a higher swirling jet ($S = 0.75$) is stronger than for a medium-swirling jet ($S = 0.3$). The difference in velocity magnitude between Reynolds number 11600 and 35000 near the impingement surface is significant for higher-swirling jets, where $Re = 35000$ shows a larger magnitude.
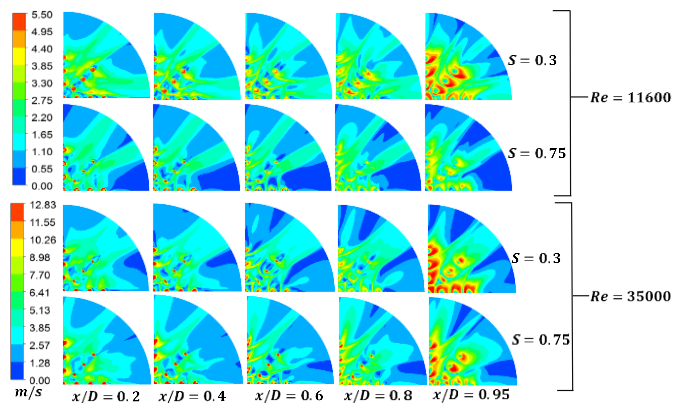
Fig. 6 Velocity contours at different axial distances of jets when $S = 0.3$ and 0.75 at $H/D = 1$ and $Re = 11600$ and 35000.

Fig. 7 shows the Nusselt number contours of adiabatic confined surface for both swirl flows at Reynolds number, $Re = 11600$, 24600, and 35000 when $H/D = 0.25$ and $r/D = 5.5$. Nusselt number is defined here as, $Nu = \frac{hD}{K}$, while h is the convective heat transfer coefficient, D is the diameter of the jet and K is the thermal conductivity of the fluid. Here, the same color scale is used for all contours. The result shows that changes

in local Nu distribution are evident only at $r/D = 0$ to 3 for all cases. Constant Nu is observed beyond that radial distance. However, these changes in heat transfer distribution due to confinement aren't evident for non-confined multiple impinging jets studies in the literature [23], [47], [48].
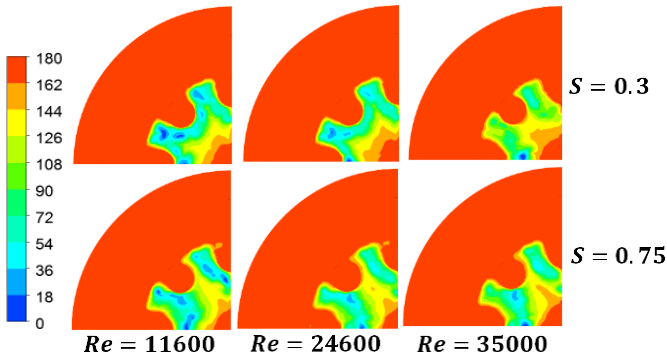
Fig. 7 Local Nusselt number recorded at confined surfaces when $S = 0.3$ and 0.75 at $H/D = 0.25$ and $Re = 11600$, 24600 and 35000.
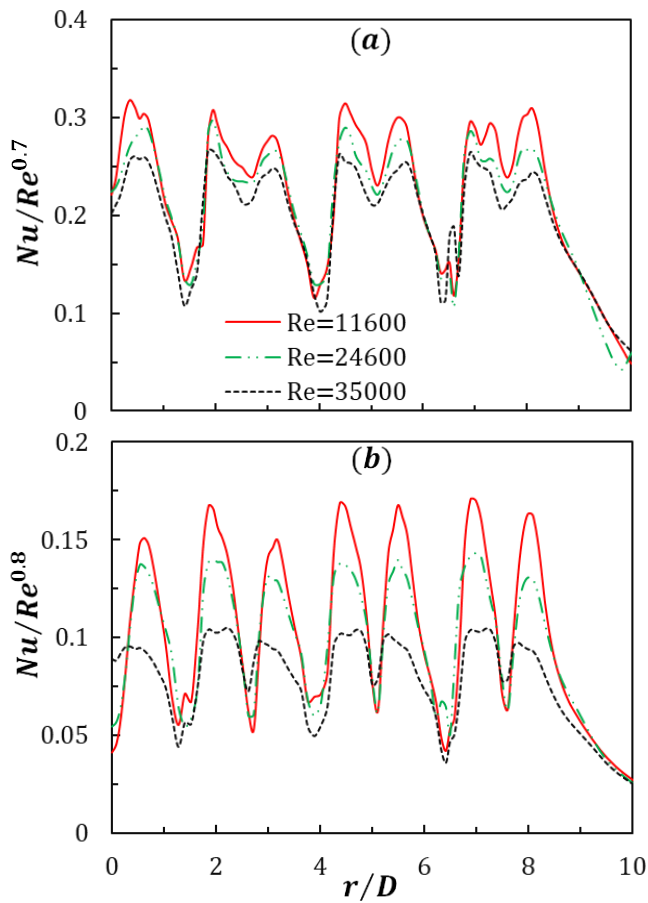
Fig. 8 The effect of Reynolds number and swirl number at $H = 0.5D$ on heat transfer distribution: (a) $S = 0.3$ and (b) $S = 0.75$.

Circumferential area-averaged surface Nusselt number ($\overline{Nu}$) is determined for all cases using Eq. (4), where A is the circumferential area on the impingement surface. Three circumferential areas of radius 8D, 12D, and 16D are chosen for their relative comparison and the results are presented in Table 2. Here, $\overline{Nu}$ decreases with the increase of averaging area, since local Nu decrease monotonically after 8D according to Fig. 8. For both medium and higher swirling cases, better heat transfer

performance is achieved for maximum Reynolds number and minimum impingement distance.

Table 2 Circumferential area-averaged Nusselt number $\overline{Nu}$ for both medium and higher swirling jets. Averaging is done for three different circumferential areas, namely 8D, 12D and 16D.

No.	S	H/D	$Re = 11600$		
			$\overline{Nu}$		
			8D	12D	16D
1		0.25	119.99	88.13	40.06
2	0.3	0.5	90.37	65.59	27.62
3		1	82.44	69.28	28.02
4		0.25	146.87	105.68	41.53
5	0.75	0.5	107.46	76.46	26.77
6		1	82.36	65.69	23.98
No.	S	H/D	$Re = 24600$		
			$\overline{Nu}$		
			8D	12D	16D
7		0.25	195.53	143.41	64.56
8	0.3	0.5	146.23	107.25	45.30
9		1	135.48	113.84	45.35
10		0.25	256.09	185.50	74.92
11	0.75	0.5	184.08	131.38	47.18
12		1	151.63	122.51	45.83
No.	S	H/D	$Re = 35000$		
			$\overline{Nu}$		
			8D	12D	16D
13		0.25	236.62	173.76	78.21
14	0.3	0.5	173.00	125.68	47.45
15		1	168.85	135.42	49.64
16		0.25	281.66	204.27	85.76
17	0.75	0.5	197.39	142.49	53.94
18		1	166.82	137.72	51.74

To analyze the effects of Reynolds number on the radial uniformity of Nusselt number distributions, Fig. 8 represents the data for swirl numbers $S = 0.3$ and 0.75 at $H = 0.5D$ ($Re = 11,600 – 35,000$). To normalize the effect of various Reynolds numbers among the data sets, radial Nu values are scaled by Re^n along the radial profile. For both medium and higher swirl flows, the values of n are respectively, n = 0.7 and 0.8 which are also implemented and proposed by literature [6], [20], [49]. Here, a slight variation in the normalized Nu exists for $S = 0.3$ at multiple radial locations. This deviation may be attributed to differing characteristics of large-scale secondary vortex rings and their influences on surface heat transfer near the impingement wall. However, in the case of higher swirl flow, greater deviations are noticeable for $Re = 35000$ from the results of $Re = 11600$ and 24600. These may be because of the formation of severer recirculation zones and strong swirl intensities in case of maximum Reynolds number and swirl number near the impingement wall. Besides, a gradual decrease of Nu is observed for all cases after 8D.

Table 3 provides information regarding thermal performance factors for different Reynolds numbers and swirl numbers at multiple impinging distances. The thermal performance factor is derived by the ratio of the relative Nusselt number to the relative friction factor as visible in Eq. (5). It is observed that maximum η is achieved at the highest impinging distances for all Reynolds numbers and swirl cases. Besides, a higher Reynolds number ensured better thermal efficiency for both medium and higher swirling flows.

Table 3 Thermal performance factors (TPF) for different cases.

Re	S	H/D	TPF
11600	0.3	0.25	0.94252
		0.5	0.88956
		1	1.17701
	0.75	0.25	1.01197
		0.5	0.95872
		1	1.34364
24600	0.3	0.25	0.98754
		0.5	1.11463
		1	1.16170
	0.75	0.25	0.89286
		0.5	0.99308
		1	1.24030
35000	0.3	0.25	1.03308
		0.5	1.18371
		1	1.24031
	0.75	0.25	1.04963
		0.5	1.21446
		1	1.58675

To analyze the effects of Reynolds number on the radial uniformity of wall pressure distributions, Fig. 9 represents the data for swirl numbers $S = 0.3$ and 0.75 at $H = 0.5D$ ($Re = 11,600 – 35,000$). As the coefficient of pressure can't be used as a dimensionless parameter to compare pressures on impingement wall surfaces at different Reynolds numbers due to the varying dynamic pressures in each case, the wall static pressure is normalized by the maximum pressure in the radial spread out for each given swirl number. The static pressure is found to be almost independent of Re for both medium and higher swirling cases when $Re = 11600$ and 24600. Here, a slight variation in the normalized P exists for $S = 0.3$ at $r/D = 0.5 – 2$; $4.5 – 5.5$, and $7 – 8$ when $Re = 35000$. For maximum ($S = 0.75$) swirl jet and $Re = 35000$, these variations are evident at $r/D = 2.5 – 3.5$; $4.5 – 5.5$, and $7.5 – 8$. These deviations may be allocated to differing properties of large-scale secondary vortex rings and their contributions to the downstream flow organization at the impingement region. No significant change in static pressure distribution is evident after $r/D = 8.5$.
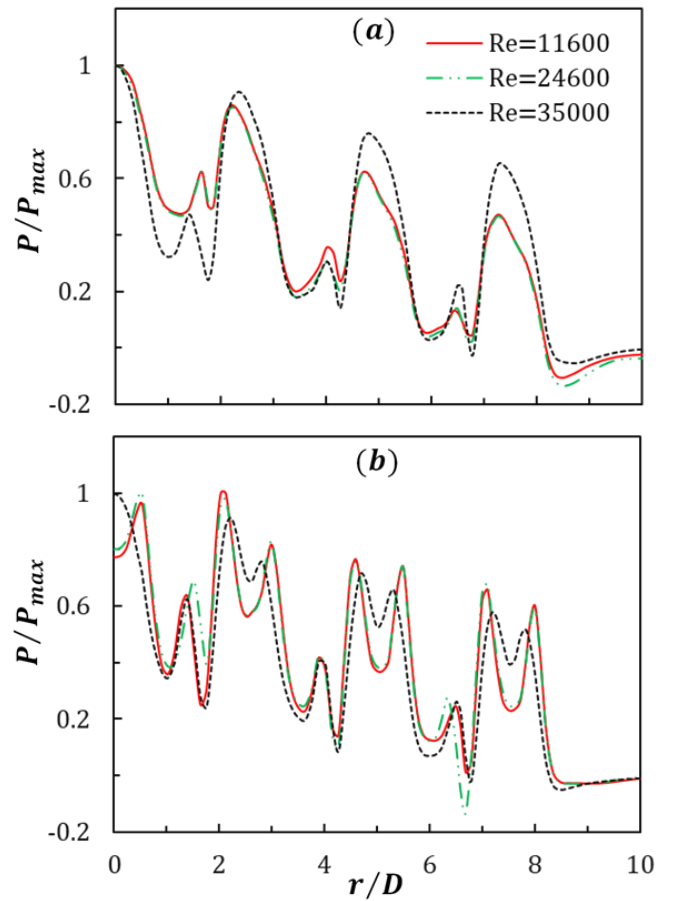
Fig. 9 The effect of Reynolds number and swirl number at $H = 0.5D$ on impingement pressure distribution: (a) $S = 0.3$ and (b) $S = 0.75$.

Fig. 10 represents the radial distribution of Reynolds normal stress along the axial direction for the inline arrangement of nozzles at $Re = 35000$ for medium ($S = 0.3$) and high swirl ($S = 0.75$) flow. It is observed that for medium swirl flow all the normal stress components $u'u'$, $v'v'$, $w'w'$ at each axial plane are maximum at the location of the nozzles and where the nozzle is not located the stress is low. Moreover, the intensity of the stress is proportional to the axial location i.e. normal stress adjacent to the plane of nozzle exit is more intense relative to the outlying planes. Due to the high flow pressure of the jet, the normal stress at the nozzle vicinity is intense. For high swirl flow, the normal shear stress shows an unpredictable nature due to the high swirl intensity. The $v'v'$, and $w'w'$ component of the normal stress are intense at the furthest position from the nozzle exit where the $u'u'$ component is intense at the $x/D = 0.5$. The magnitude of normal shear stress is found maximum adjacent to the 3rd and 4th series of nozzles, where at the first and second nozzle the stress is not intense. This can be attributed to the strong recirculation vortex due to the high swirl flow which occurs at $r/D = 4-5$ and $6.5-7.5$.
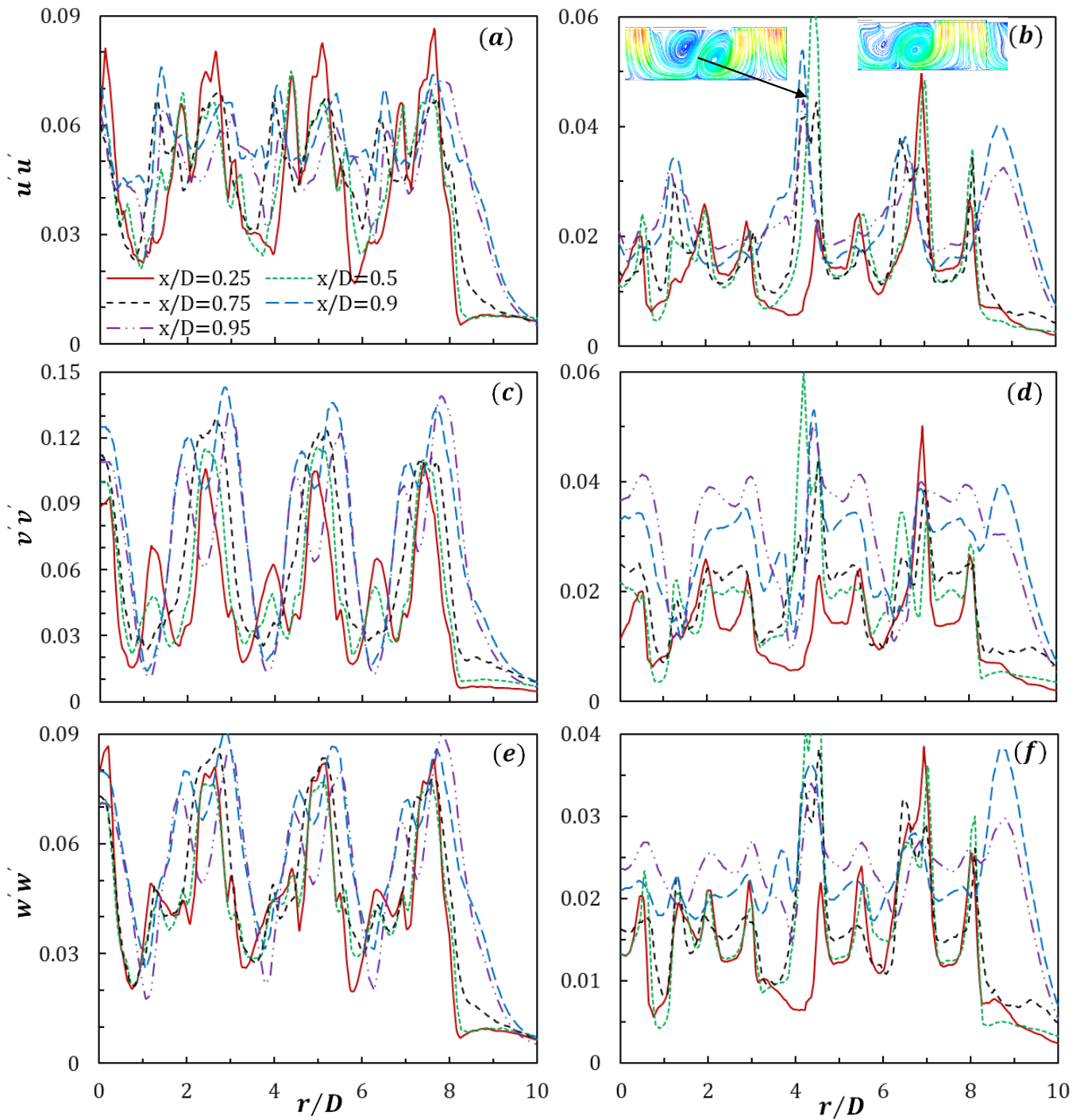
Fig. 10 Radial distribution of Reynolds normal stress along different axial planes at $Re = 35000$ and $H/D = 1$ for (a, c, e) $S = 0.3$ and (b, d, f) $S = 0.75$.

Fig. 11 represents the radial distribution of Reynolds shear stress along the axial direction for the inline arrangement of nozzles at $Re = 35000$ at $H/D = 1$ for medium ($S = 0.3$) and high swirl ($S = 0.75$) flow. It is observed that the Reynolds shear stress shows a very unpredictable nature due to the effect of the swirl. The $u'v'$ component of shear stress at $x/D = 0.5$ is comparatively more intensive than other locations for medium swirl flow. The magnitude of shear stress $u'v'$ component at the nozzle location is low. On the contrary, in the case of high swirl flow the $u'v'$ component of shear stress at $x/D = 0.9$ is more intensive.

However, near the 3rd series of the nozzle the $u'v'$ component of shear stress at $x/D = 0.25$ and $x/D = 0.5$ suddenly become high. The $u'w'$ component of shear stress at the nozzle location is high for both medium and high swirl flow conditions. Moreover, the magnitude of the stress at the vicinity of the nozzle exit is more intense compared to the outlying planes. The $v'w'$ component of shear stress is minimum at the nozzle location for medium swirl flow and the intensity of the stress near the nozzle exit plane is high. For high swirl flow, the stress at $r/D = 5$-7 suddenly becomes very high.
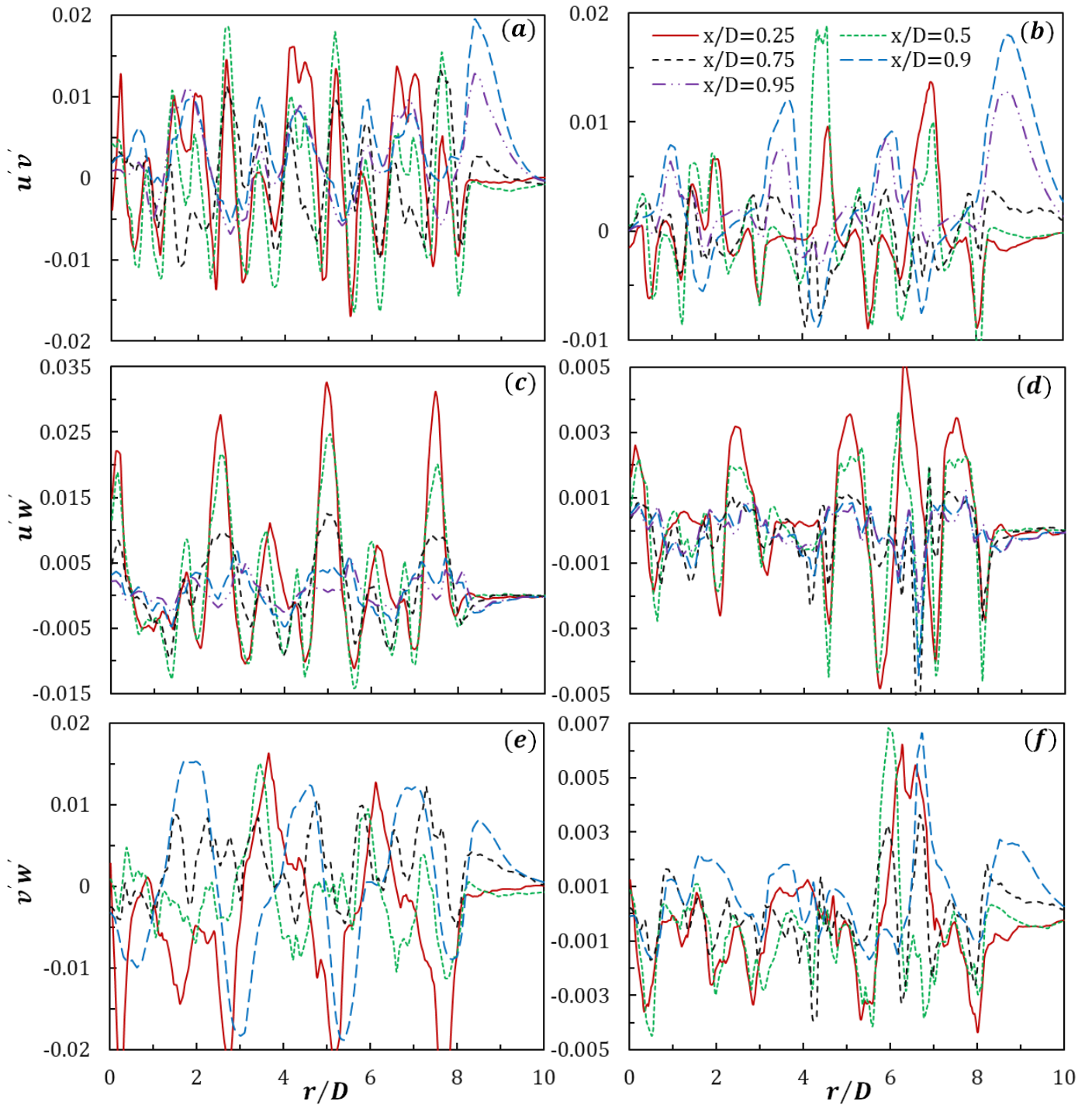
Fig. 11 Radial distribution of Reynolds shear stress along the axial direction of the impinging plate at *Re*= 35000 at *H/D* = 1 for (a, c, e) *S* = 0.3 and (b, d, f) *S* = 0.75.

Heat transfer for all cases is predicted by using multivariate regression analysis on the commercial software package IBM SPSS. The proposed correlation relates to all Reynolds numbers, impinging distances, and swirl numbers. The founded correlation equation for area average $\overline{Nu}$ is given as Eq. (6). Fig. 12 portrayed the virtue of every fit by plotting ±10% error bands with comparisons between the numerical values and predicted ones by Eq. (6). The obtained R^2 value for the correlation is 0.952 and it is visible that, most predictions stay within both error bands. This shows that the proposed correlation is acceptable for the considered cases in the current study. Numerous cases are considered in the current study along with the different flow and geomatics parameters. Consequently, it's necessary to investigate the outcomes in terms of possible enhancement factors. As such, the Circumferential area-averaged surface Nusselt number ($\overline{Nu}$) and thermal performance factor (TPF) are tested for an increase of swirl intensity from medium ($S = 0.3$) to high ($S = 0.75$), while $Re = 11600$ and $H/D = 0.5$. 19% and 8% raises are predicted in terms of $\overline{Nu}$ and TPF respectively. Furthermore, both parameters are tested with the change of Reynolds number from 11600 to 35000 while $S = 0.75$ and $H/D = 1$. Around 102% and 23% increments are found in terms of $\overline{Nu}$ and TPF respectively.
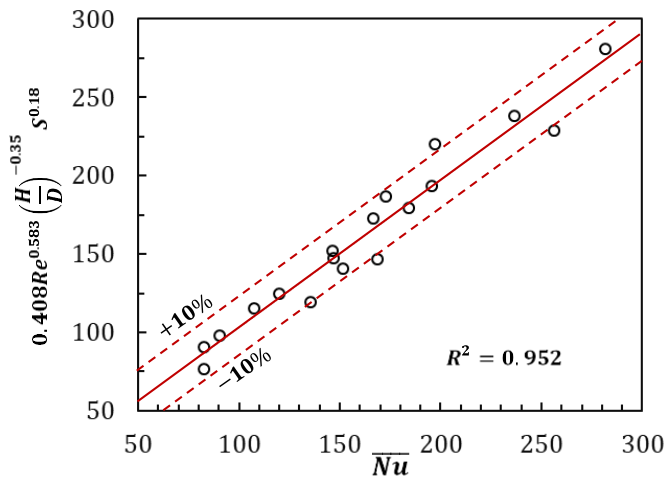
Fig. 12 Contrast among the simulation data and the correlated results for area average Nusselt number (*Nu*) with error bands.

5 Conclusion

A numerical study has been conducted to investigate the thermo-fluidic characteristics of a swirl-impinging jet emanating from an aerodynamic swirl nozzle for various flow and geometric conditions. The flow parameters are selected based on Reynolds numbers, impinging distance, swirl number, and jet-to-jet separation distances. The analysis is conducted using the SST k-ω turbulence model, and various flow and thermal behaviors are observed. The results of this analysis are summarized below:

- The static pressure at the stagnation region is very high for both the low and high swirl flows and gradually decreases with the radial and circumferential distance. Moreover, static pressure adjacent to the nozzle exit is low and increases gradually with the impinging distance. Pressure distribution along the impingement surface is more uniform in case of high swirl flow. Besides, the static pressure is found independent of the Reynolds number for both the low and high swirl flow at a low Reynolds number. However, for a high Reynolds number, significant variation of static pressure is observed due to the influence of the large-scale secondary vortex downstream to the impingement region.

- The jet velocity is maximum at the vicinity of the nozzle exit and decelerates gradually towards the impingement surface. This receding tendency is relatively stronger for high swirl flow than the low swirl conditions.

- Local Nusselt number at the confinement surface is varying at a radial distance of 0 to 3 for all the flow conditions and beyond that distance, the Nusselt number is found constant. Moreover, the heat transfer characteristic at the confined surface is different from the non-confined ones. Nusselt number at the stagnation region is very high which accelerates with the Reynolds number and swirl number due to the increased flow velocity and turbulence, respectively. The average Nusselt number decreases with the increment of the circumferential area on the impinging surface and maximum heat transfer performance is evident at the minimum impinging distance. Moreover, a correlation is established for the area average Nusselt numbers for all the considered cases in the current study.

- Reynolds normal stress adjacent to the nozzle exit is more intensive compared to the outlying planes due to the high flow pressure of the jet while the Reynolds shear stress along the radial direction is changing unpredictably due to the influence of the recirculating vortex.

- An estimated 102% enhancement in average Nusselt number is observed for high swirl flow, at a Reynolds number increment from 11600 to 35000. This enhancement is evident by 23% in terms of thermal performance factor. Besides, the average Nusselt number and thermal performance factor augmented by 19% and 8%, respectively, for an increased swirl intensity at low a Reynolds number (*Re* =11600).

References

[1] Röger, M., Buck, R. and Müller-Steinhagen, H., 2005. Numerical and experimental investigation of a multiple air jet cooling system for application in a solar thermal receiver.

[2] Han, J.C., 2004. Recent studies in turbine blade cooling. *International journal of rotating machinery*, *10*(6), pp.443-457.

[3] Becko, Y., 1976. Impingement Cooling—A Review, *Von Karman Institute for Fluid Dynamic*, Lecture Series 83, Turbine Blade Cooling.

[4] Hall, C.W., 1988. Handbook of industrial drying, *Dry. Technol. 6*(3), pp. 571–573.

[5] Yang, L., Ren, J., Jiang, H. and Ligrani, P., 2014. Experimental and numerical investigation of unsteady impingement cooling within a blade leading edge passage. *International Journal of Heat and Mass Transfer*, *71*, pp.57-68.

[6] Martin, H., 1977. Heat and mass transfer between impinging gas jets and solid surfaces. In *Advances in Heat Transfer,* 13, pp. 1-60, Elsevier.

[7] Colucci, D.W. and Viskanta, R., 1996. Effect of nozzle geometry on local convective heat transfer to a confined impinging air jet. *Experimental Thermal and Fluid Science*, *13*(1), pp.71-80.

[8] Saad, N.R., Polat, S. and Douglas, W.J.M., 1992. Confined multiple impinging slot jets without crossflow effects. *International Journal of Heat and Fuid Flow*, *13*(1), pp.2-14.

[9] Huber, A.M. and Viskanta, R., 1994. Convective heat transfer to a confined impinging array of air jets with spent air exits. *J. Heat Transfer*, *116*(3), pp. 570-576.

[10] Markal, B., 2018. Experimental investigation of heat transfer characteristics and wall pressure distribution of swirling coaxial confined impinging air jets. *International Journal of Heat and Mass Transfer*, *124*, pp.517-532.

[11] Markal, B., 2019. The effect of total flowrate on the cooling performance of swirling coaxial impinging jets. *Heat and Mass Transfer*, *55*(11), pp.3275-3288.

[12] Habib, M.A. and Whitelaw, J.H., 1980. Velocity characteristics of confined coaxial jets with and without swirl. *J. Fluids Eng*. *102*(1), pp. 47-53.

[13] Memar, H., Holman, J.P. and Dellenback, P.A., 1993. The effect of a swirled annular jet on convective heat transfer in confined coaxial jet mixing. *International Journal of Heat and Mass Transfer*, *36*(16), pp.3921-3930.

[14] Petera, K. and Dostál, M., 2017. Heat transfer in a confined impinging jet with swirling velocity component. In *EPJ Web of Conferences,* 143, p. 02091. EDP Sciences.

[15] Shuja, S.Z., Yilbas, B.S. and Rashid, M., 2003. Confined swirling jet impingement onto an adiabatic wall. *International Journal of Heat and Mass Transfer*, *46*(16), pp.2947-2955.

[16] Chouaieb, S., Kriaa, W., Mhiri, H. and Bournot, P., 2017. Swirl generator effect on a confined coaxial jet characteristics. *International Journal of Hydrogen Energy*, *42*(48), pp. 29014-29025.

[17] Liu, L., Zhang, J., Liu, S., Wang, K. and Gu, H., 2021. Decay law and swirl length of swirling gas-liquid flow in a vertical pipe. *International Journal of Multiphase Flow*, *137*, p.103570.

[18] Yan, J., Gui, N., Xie, G. and Gao, J., 2014. Direct numerical simulation and visualization of biswirling jets. *Advances in Mechanical Engineering*, *6*, p.193731.

[19] Fénot, M., Dorignac, E. and Lalizel, G., 2015. Heat transfer and flow structure of a multichannel impinging jet. *International Journal of Thermal Sciences*, *90*, pp.323-338.

[20] Ahmed, Z.U., Al-Abdeli, Y.M. and Guzzomi, F.G., 2017. Flow field and thermal behaviour in swirling and non-swirling turbulent impinging jets. *International Journal of Thermal Sciences*, *114*, pp.241-256.

[21] Ahmed, Z.U., Al-Abdeli, Y.M. and Matthews, M.T., 2015. The effect of inflow conditions on the development of non-swirling versus swirling impinging turbulent jets. *Computers & Fluids*, *118*, pp.255-273.

[22] Wu, F., Li, L., Wang, J., Fan, X. and Du, C., 2019. Numerical investigations on flow and heat transfer of swirl and impingement composite cooling structures of turbine blade leading edge. *International Journal of Heat and Mass Transfer*, *144*, p. 118625.

[23] Debnath, S., Khan, M.H.U. and Ahmed, Z.U., 2020. Turbulent swirling impinging jet arrays: A numerical study on fluid flow and heat transfer. *Thermal Science and Engineering Progress*, *19*, p. 100580.

[24] Debnath, S., Khan, M.H.U., Ahmed, Z.U. and Alam, M.M., 2018. The effect of swirl on array of turbulent impinging jets. In *International Conference on Mechanical, Industrial and Energy Engineering,* December, 2018, Khulna, Bangladesh.

[25] Debnath, S. and Ahmed, Z.U., 2020. Computational analysis of multiple non-swirling & swirling impinging air jets. In *International Conference on Mechanical, Industrial and Energy Engineering*, December, Khulna, Bangladesh.

[26] Wannassi, M. and Monnoyer, F., 2015. Fluid flow and convective heat transfer of combined swirling and straight impinging jet arrays. *Applied Thermal Engineering*, *78*, pp.62-73.

[27] Hollworth, B.R., Lehmann, G. and Rosiczkowski, J., 1983. Arrays of impinging jets with spent fluid removal through vent holes on the target surface, part 2: local heat transfer.

[28] Zhang, J., Sun, Y., Li, J. and He, X., 2020. Study on the hybrid cooling of the flame tube in a small triple-swirler combustor. *Energies*, *13*(21), p. 5554.

[29] Wu, F., Li, L., Wang, J., Fan, X. and Du, C., 2019. Numerical investigations on flow and heat transfer of swirl and impingement composite cooling structures of turbine blade leading edge. *International Journal of Heat and Mass Transfer*, *144*, p. 118625.

[30] Caliskan, S. and Baskaya, S., 2012. Experimental investigation of impinging jet array heat transfer from a surface with V-shaped and convergent-divergent ribs. *International Journal of Thermal Sciences*, *59*, pp. 234-246.

[31] Chauhan, R. and Thakur, N.S., 2013. Heat transfer and friction factor correlations for impinging jet solar air heater. *Experimental Thermal and Fluid Science*, *44*, pp.760-767.

[32] Hatami, M., Bazdidi-Tehrani, F., Abouata, A. and Mohammadi-Ahmar, A., 2018. Investigation of geometry and dimensionless parameters effects on the flow field and heat transfer of impingement synthetic jets. *International Journal of Thermal Sciences*, *127*, pp.41-52.

[33] Wang, C., Wang, Z., Wang, L., Luo, L. and Sundén, B., 2019. Experimental study of fluid flow and heat transfer of jet impingement in cross-flow with a vortex generator pair. *International Journal of Heat and Mass Transfer*, *135*, pp. 935-949.

[34] Katti, V.V., Yasaswy, S.N. and Prabhu, S.V., 2011. Local heat transfer distribution between smooth flat surface and impinging air jet from a circular nozzle at low Reynolds numbers. *Heat and Mass Transfer*, *47*(3), pp. 237-244.

[35] Jeffers, N., Stafford, J., Conway, C., Punch, J. and Walsh, E., 2016. The influence of the stagnation zone on the fluid dynamics at the nozzle exit of a confined and submerged impinging jet. *Experiments in Fluids*, *57*(2), pp. 1-15.

[36] Ekkad, S.V. and Han, J.C., 2000. A transient liquid crystal thermography technique for gas turbine heat transfer measurements. *Measurement Science and Technology*, *11*(7), p. 957.

[37] Ichikawa, Y., Motosuke, M., Kameya, Y., Yamamoto, M. and Honami, S., 2016. Three-dimensional flow characterization of a square array of multiple circular impinging jets using stereoscopic PIV and heat transfer relation. *Journal of Visualization*, *19*(1), pp. 89-101.

[38] Buzzard, W.C., Ren, Z., Ligrani, P.M., Nakamata, C. and Ueguchi, S., 2017. Influences of target surface small-scale rectangle roughness on impingement jet array heat transfer. *International Journal of Heat and Mass Transfer*, *110*, pp. 805-816.

[39] Ligrani, P.M., Ren, Z. and Buzzard, W.C., 2017. Impingement jet array heat transfer with small-scale cylinder target surface roughness arrays. *International Journal of Heat and Mass Transfer*, *107*, pp. 895-905.

[40] Singh, D., Premachandran, B. and Kohli, S., 2015. Circular air jet impingement cooling of a circular cylinder with flow confinement. *International Journal of Heat and Mass Transfer*, *91*, pp. 969-989.

[41] Caggese, O., Gnaegi, G., Hannema, G., Terzis, A. and Ott, P., 2013. Experimental and numerical investigation of a fully confined impingement round jet. *International Journal of Heat and Mass Transfer*, *65*, pp. 873-882.

[42] Manca, O., Cirillo, L., Nardini, S., Buonomo, B. and Ercole, D., 2016. Experimental investigation on fluid dynamic and thermal behavior in confined impinging round jets in aluminum foam. *Energy Procedia*, *101*, pp. 1095-1102.

[43] Islam, S.M., Khan, M.T. and Ahmed, Z.U., 2020. Effect of design parameters on flow characteristics of an aerodynamic swirl nozzle. *Progress in Computational Fluid Dynamics, an International Journal*, *20*(5), pp. 249-262..

[44] Khan, M.T., Islam, S.M. and Ahmed, Z.U., 2020. Near-wall and turbulence behavior of swirl flows through an aerodynamic nozzle. *Journal of Engineering Advancements*, *1*(2), pp. 43-52.

[45] Khan, T. and Ahmed, Z.U., 2022. Effect of nanofluids on heat transfer characteristics of an aerodynamic swirl nozzle for isothermal and isoflux conditions. *Australian Journal of Mechanical Engineering*, pp. 1-19.

[46] Ahmed, Z.U., 2016. An experimental and numerical study of surface interactions in turbulent swirling jets. *Dissertation submitted for the degree of Doctor of Philosophy, School of Engineering*, Edith Cowan University, Australia.

[47] Debnath, S., Ahmed, Z.U., Ikhlaq, M. and Khan, T., Thermal characteristics of arrays of swirling impinging jets: Effect of Reynolds number, impingement distance, and jet-to-jet separation. *Heat Transfer*, *51*(1), pp. 585-608.

[48] Khan, T., Debnath, S., Ahmed, Z. U., & Islam, S.M., 2022. Effects of impinging distance, reynolds number, and swirl on the flow and heat transfer behaviors of arrays of circular impinging jets: A numerical approach. In *International Conference on Mechanical, Industrial and Energy Engineering* December, Khulna, Bangladesh.

[49] Ahmed, Z.U., Al-Abdeli, Y.M. and Guzzomi, F.G., 2016. Heat transfer characteristics of swirling and non-swirling impinging turbulent jets. *International Journal of Heat and Mass Transfer*, *102*, pp. 991-1003.

Design of a Smart Biofloc Monitoring and Controlling System using IoT

Rumana Tasnim[1], Abu Salman Shaikat[1,], Abdullah al Amin[1], Molla Rashied Hussein[2], Md Mizanur Rahman[1]*

[1]Department of Mechatronics Engineering, World University of Bangladesh (WUB), Dhaka-1205, Bangladesh
[2]Department of Computer Science & Engineering, University of Asia Pacific (UAP), Dhaka-1205, Bangladesh

ABSTRACT

In this paper, an IoT based real-time monitoring and controlling system have been designed and developed for an eco-friendly aquaculture system namely a biofloc fish farm. Currently, technology has a vital role in improving aquaculture production which leads to attaining sustainable development. The microorganisms in the biofloc fish tank are utilized for detoxifying the toxic waste materials by recycling as well as transforming them into fish food e.g. protein cells. Hence, it not only manages good water quality in the biofloc system but also produces additional feed for the fish. Water quality monitoring of biofloc fish tanks is a significant aspect to guarantee a better environment for producing fish. This paper focuses on developing an IoT based device for biofloc fish tanks to monitor various water quality parameters as well as control water temperature and air pump. Using this device, users can monitor the water quality data received from sensors and control the actuators accordingly from any remote location through the graphical user interface (GUI).

Keywords: Aquaculture, Monitoring, Controlling, Biofloc, Turbidity, Temperature.

1 Introduction

Biofloc aquaculture has been proliferating around the world in recent times. This system allows producing an increased amount of food from the smaller area of land with fewer inputs. In this system, the cost of fish feeds is decreased since the toxic waste nutrients are converted and consumed by fish later on. The use of aggregates of bacteria, algae, or protozoa enhances water quality, ensures waste treatment, and prevents disease in the aquaculture system. The traditional fish farm has a number of issues namely temperature instability, nutrition, water pollution, high maintenance charge, etc. In fish farming, biofloc technology transforms the conventional fish farming process into another infrastructure that utilizes the leftover food by converting it into bacterial biomass. Crab et al. [1] conducted a review of the advantageous effects of the biofloc process and addressed a number of challenges for further research. Hargreves et al. [2] referred to biofloc technology as a technique to enhance ecological control over production. Researchers and engineers designed a variety of monitoring and controlling systems for the fish farm over recent years. Phawa et al. [3] designed and developed an automated biofloc fish farming system. For measurement of the water temperature, a temperature sensor has been used. Arduino board is used for processing and controlling a heater that is placed in the tank. Furthermore, Mahanjan et al. [4] developed an e-monitoring system for the automated fish farming process. This system is integrated with IoT supported system for monitoring the fish farming process where PH sensors, Temperature sensors, TDS sensors, and Gas sensors were used. Noor et al. [5] developed a PIC microcontroller based automatic fish feeding system. The rotational speed of the DC motor controls the pellets in the automated fish feeding system. Another research by Tasin et al. [6] focussed on IoT based monitoring and assessing the quality of river water for saving the ecosystem. The researchers developed an Artificial Neural Network (ANN) based automated device with the help of IoT.

Parra et al. [7] developed a wireless sensor network based approach to monitor both the fish behavior as well as water quality in an aquaculture tank using a low-cost sensor system. Their proposed system is capable of monitoring the status of the fish tank, the velocity and depth of feed falling and fish swimming along with the water quality parameters as well. A. Ramya et al. [8] developed another IoT based automated system that can not only monitor the fish farm but also assists the fish farm owners to maintain the fish feeding process. Shaari et al. [9] proposed an integrated system that combines both the automatic feed dispensing as well as distribution process. Kayalvizhi et. al. [10] proposed an automated device integrating sensors such as TDS sensor, pH sensor, Dissolved oxygen and Ultrasonic sensor, and controllers like Raspberry Pi and Arduino board. Chen et al. [11] conducted a thorough experiment on some water quality parameters namely pH, temperature, and dissolved oxygen developing an automated monitoring system that could work wirelessly via the Zigbee sensor network. Further research work by H Hendri et al. [12] demonstrated an automatic fish feeding approach where the turbidity level of water is tested and Arduino Mega was used as a controller. Research by Phillip G Lee et al. [13] focussed on developing bio-filters for monitoring water parameters. The authors made use of video cameras inside the fish tank to check the status and growth of the fish. Garcia-Pineda et al. [14] developed a cost effective automated fish feeding control system using a set of sensors. Bhakti et al. [15] highlighted analyzing water quality by measuring temperature, TDS, turbidity, and pH with various sensors and Raspberry Pi controllers. Mozumder et al. [16] proposed a smart IoT based biofloc monitoring system that uses a number of sensors that collect, store, and analyze the sensed data by using the decision regression tree model for forecasting the water condition. Rashid et al. [17] presented an IoT based water quality prediction system using sensors and carried out a machine learning based analysis for tracing water quality and sending notifications to the user as well. Yang et al. [18] developed a smart prototype system for

classifying dead and live fish species and evaluating feeding decisions using the deep learning approach. However, this system could not address composite data in aquaculture. Dzulqornain et al. [19] proposed an automated IoT based approach and implemented the machine learning algorithm for the prediction of the quality of water in the biofloc tank. The proposed approach uses some parameters such as pH, temperature, turbidity, and total dissolved solids, and the sensor data was stored in the cloud. However, the process was manual. Ahmed et al. [20] implemented a prototype of a biofloc farm monitoring system taking into consideration of the chemical properties of water and controlling the pumps as well. A mobile application was used for real-time monitoring and controlling as well. However, the system performance was not evaluated.

From the thorough review of related literature, it is obvious that the water quality is based mainly on some crucial water parameters namely pH, temperature, turbidity, total dissolved solids, etc. In this work, an IoT based system has been developed which has real-time monitoring data on water quality and these data are ultimately sent to the cloud. Furthermore, the temperature of the water tank is controlled along with the air pump as well.
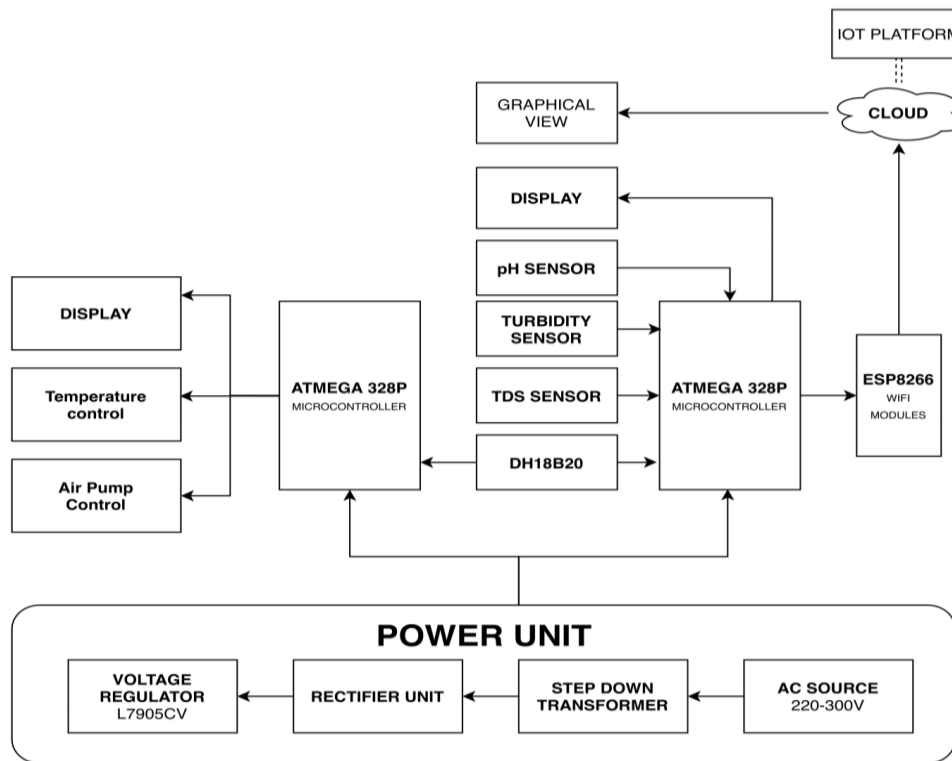
Fig. 1 System block diagram.

2 System Design

Fig. 1 illustrates the system block diagram. In this diagram, the power unit is comprised of an AC voltage source which is transformed into a DC voltage source with the help of a rectifier. The device is comprised of Atmega 328P microcontroller, Node MCU, pH Sensor - pH-4502C, Temperature sensor - DH18B20, turbidity sensor, TDS sensor, LCD Monitor, and Air pump. Atmega 328P is used with ESP8266 module that links the embedded device to the internet and gathers the relevant data from temperature (DS18B20), analog pH, TDS, and turbidity sensors. These sensed data go to the microcontroller. Depending on the water quality and water temperature in the tank, the microcontroller sends a trip signal to the relay. Then the heating rod, as well as the water pump, is both turned ON. The Atmega 328P acts as a sensor node assuring continuous data transmission through ESP8266. Moreover, the received data are transmitted to the web server "Thinger.io". Air pumps are also one of the key parts of the developed system to supply oxygen which is controlled as well. Adding the GUI (Graphical User Interface) is another essential part of the Thinger.io application.Three Atmega328P are used for carrying out a number of tasks. The developed device not only controls temperature and air pump,

but also monitors the quality of water and processes the analog data. Fig. 2 shows the circuit diagram. Fig. 3 represents the flow chart. The temperature sensor (DS18B20) detects the water temperature and displays it on the monitor. If the temperature becomes less than the value set by the user, then the microcontroller sends a trip signal to relay for turning ON the heating rod as well as the water pump. If the temperature of the water becomes equal to the set value, it resends the trip signal to the relay for switching ON the heating rod and turning OFF the water Pump. Users are allowed to fix the value of temperature and the entire procedure is repeated. Also, both air pumps are initiated. If the first pump is turned ON, then the second pump is turned OFF. After a preset amount of "X" delay, the first air pump is turned OFF and the second air pump is also turned ON and the entire procedure is repeated. A user can fix the time value "X". Data received from the sensors is in the millivolt range. In the biofloc aquaculture system, the range of analog pH is from 0 to 14, the TDS sensor is from 50 to 2000 ppm, Turbidity is from 0 to 3000 NTU and DS18B20 sensor is from -55 to 155 degrees Celsius. If the received data from the sensor fulfills the program condition, then the display shows the data which are sent to the cloud.
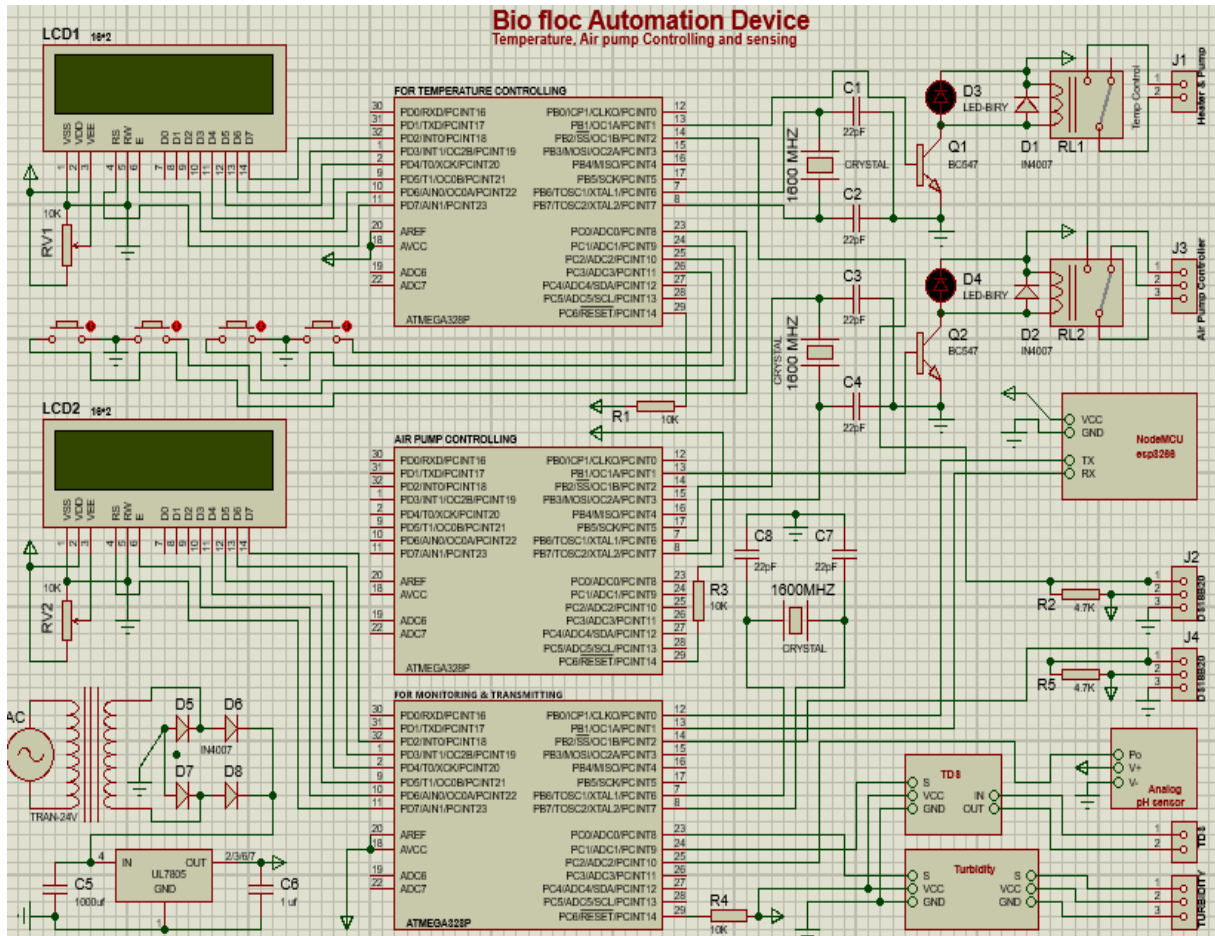
Fig. 2 Circuit diagram.
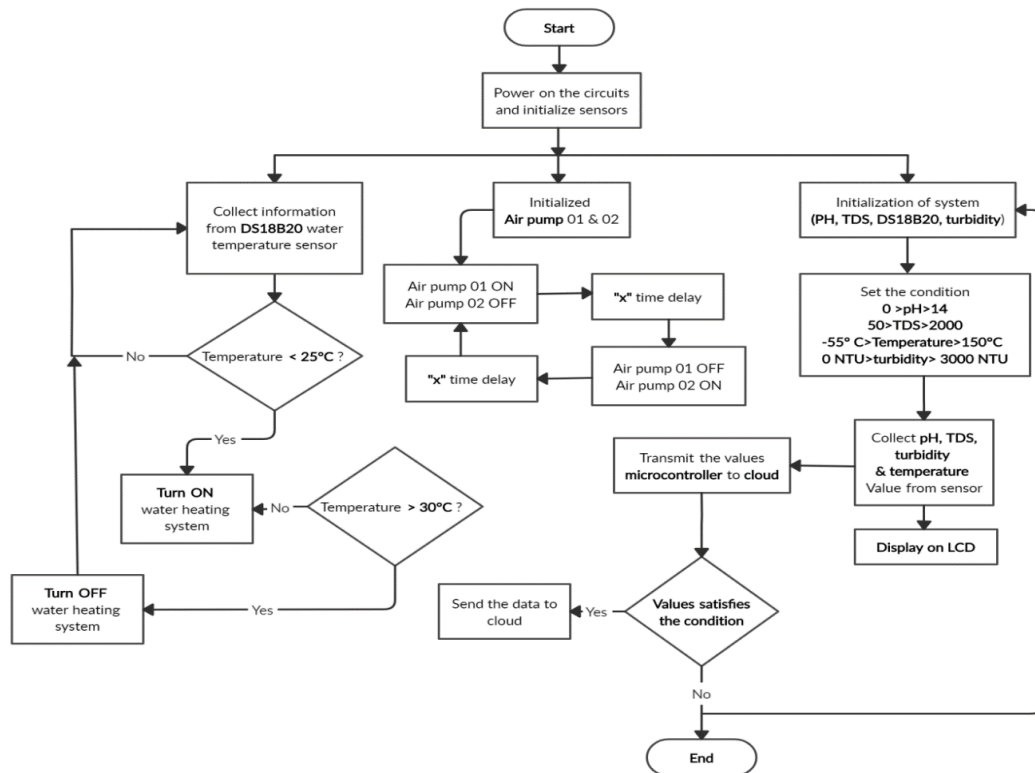
Fig. 3 Flow chart.

3 System Setup

A biofloc fish tank was selected for the purpose of experimentation which can contain 10,000 litres. Fig. 4 illustrates the entire setup.
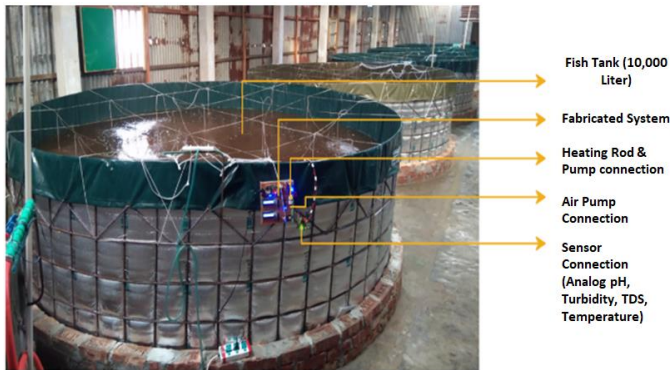
Fig. 4 Device setup.

Fig. 5 demonstrates the entire hardware setup which has a power supply unit, sensor unit, capacitor, relay, as well as a control unit. There are air pumps, a heating rod, and ESP8266 in the controlling unit. Fig. 6 shows the complete sensor connection in the biofloc tank. There are two LCD displays that present the measured value.
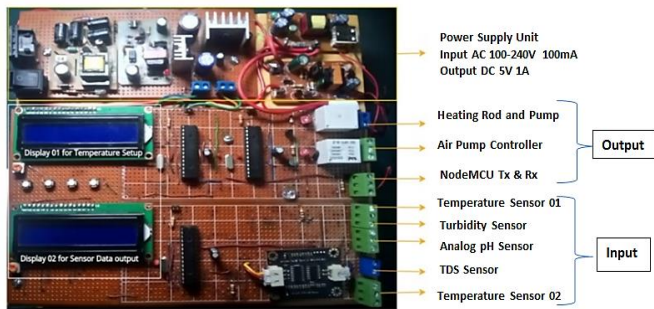
Fig. 5 Hardware setup.
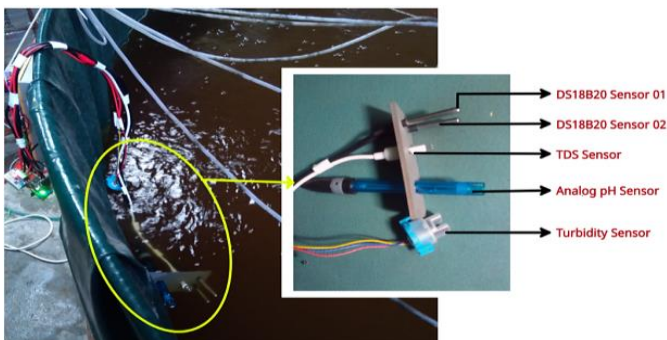
Fig. 6 Sensor connection in tank.

4 Results Analysis

For controlling water temperature, the experiment is conducted with the help of a heating rod. The relay remains normally open (NO). Based on the temperature, trip signals are sent from the microcontroller (Atmega328P) that ground the relay through an NPN transistor (BC547). Thus, the heating rod is turned ON and the user can easily set the time delay. The experimental result demonstrates that if the temperature of the water becomes less than 25° Celsius, then the microcontroller sends the trip signal which turns ON the heating rod as well as

the water pump. If the water temperature becomes 30° Celsius, then the relay becomes tripped again and the heating rod as well as the water pump becomes ultimately turned OFF. The temperature sensor (DS18B20 sensor) senses the water temperature. The received dataset was recorded at room temperature. The timing of the air pump is also controlled by setting the 'X' time delay. The experimental results were received successfully.

In this work, an analog pH sensor, Turbidity sensor, TDS sensor, and Temperature (DS18B20) sensor were used for sensing the quality of water in the fish tank. For biofloc fish farming, a pH value of less than 7.0 is preferable. From the measured pH values, the system takes the data from the pH sensor as well as calculates it which is shown in LCD (16*2) display. Simultaneously, these data are sent to the Thinger.io webserver. When the pH value becomes more than the reference level (more than 8), then the water becomes alkane. However, when the level is less than 6.8, then the water becomes acidic. As soon as the water turns acidic, a warning message is shown on the display. Users can check the data by monitoring the level and subsequently taking the required action. Fig. 7(a) shows the pH level while Fig. 7(b) represents the level of water temperature on the LCD monitor.

(a)

(b)

Fig. 7 Measuring water quality (a) pH value and warning message (b) water temperature.

(a)

(b)

Fig. 8 Water quality data (a) TDS level (b) Turbidity level.

TDS sensor measures the amount of total dissolved solids in water. The TDS data is gathered using a TDS sensor and sent to the TDS module which transmits the data to the microcontroller. Then the TDS sensor values are seen in the LCD display. In this work, a turbidity sensor is also used to measure the purity of the water. LCD display shows the measured values of turbidity as the water becomes very clean. Fig. 8(a) and Fig. 8(b) illustrate both the TDS level and turbidity level of water.

Table 1 shows the experimental data of measurements taken from the biofloc fish tank over 15 hours. These data changed according to time indicating the changes in water quality parameters.

It is apparent that the value of pH is changing from 5.5 to 6.8. It represents that the water is transforming from acidic to alkane condition. When the pH value is below 7, it means that the water is acidic. Furthermore, from Table 1, it can be seen that the amount of dissolved solid varies from time to time. Also, the temperature of the water depends on the weather and environment. The minimum temperature recorded was 23 °C which was observed in the early morning and the highest one was 31°C which was observed in the midday. Moreover, the turbidity values change from time to time based on the cleanliness of the water.

5 Real-time monitoring

Real-time monitoring was carried out for pH, TDS, and water temperature levels. In this work, a cloud IoT Platform named Thinger.io was used. By using the IoT Platform, any user can observe the water quality parameters from anywhere in the world. The server shows the stored real-time data. Users can also download the data if necessary. Fig. 9 illustrates the graphical representation of the real-time data for pH whereas Fig. 10(a) illustrates the exact value anytime in an instant using the Gooch chart. Likewise, Fig. 11 illustrates the graphical representation of TDS values in real-time while Fig. 10(b) shows the Gooch chart. Also, Fig. 12 illustrates the real-time temperature data of tank water whereas Fig. 10(c) represents the gooch chart of temperature data.

Table 1 Sensor output during the experiment in the biofloc system.

Time in hours	pH	Temperature (°C)	Turbidity (NTU)	Total Dissolved Solid (PPM)
7:00 AM	6.7	23	7	220
8:00 AM	6.7	23	7	223
9:00 AM	6.8	24	8	227
10:00 AM	6.5	25	8	222
11:00 AM	6.0	27	7	230
12:00 PM	5.8	30	7	229
01:00 PM	5.5	31	8	233
02:00 PM	5.5	31	7	228
03:00 PM	5.4	30	8	227
04:00 PM	5.7	28	8	230
05:00 PM	5.9	26	7	234
06:00 PM	6.1	25	7	230
07:00 PM	6.5	25	8	237
08:00 PM	6.8	25	8	237
09:00 PM	6.9	24	7	240
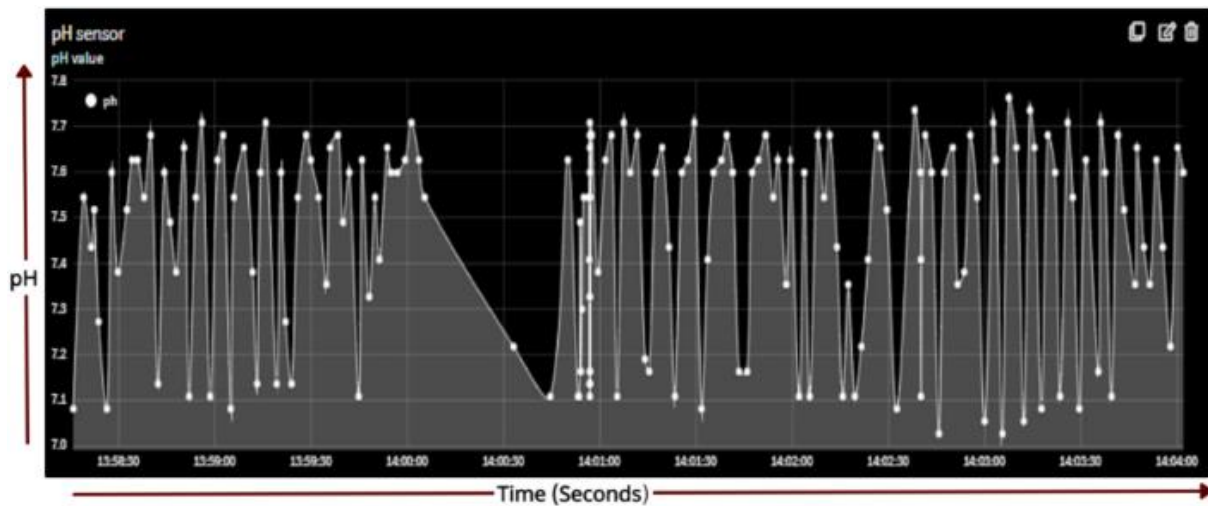
Fig. 9 Real-time graph of analog pH.

| (a) | (b) | (c) |
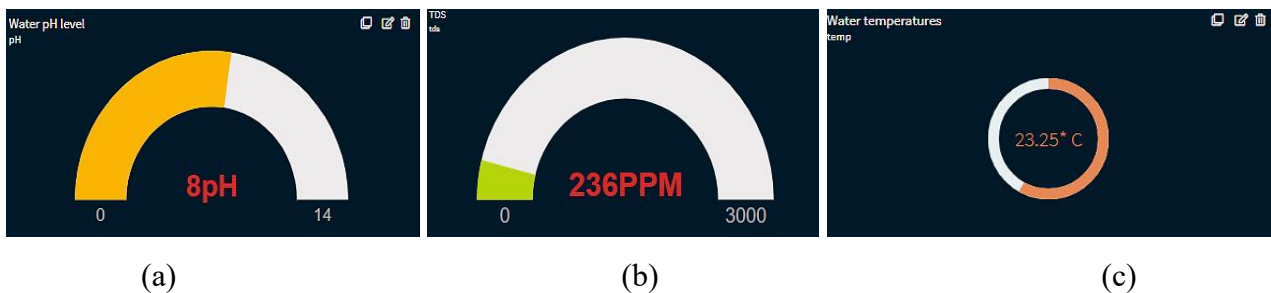
Fig. 10 Gooch chart for (a) pH, (b) TDS, and (c) Water temperature.
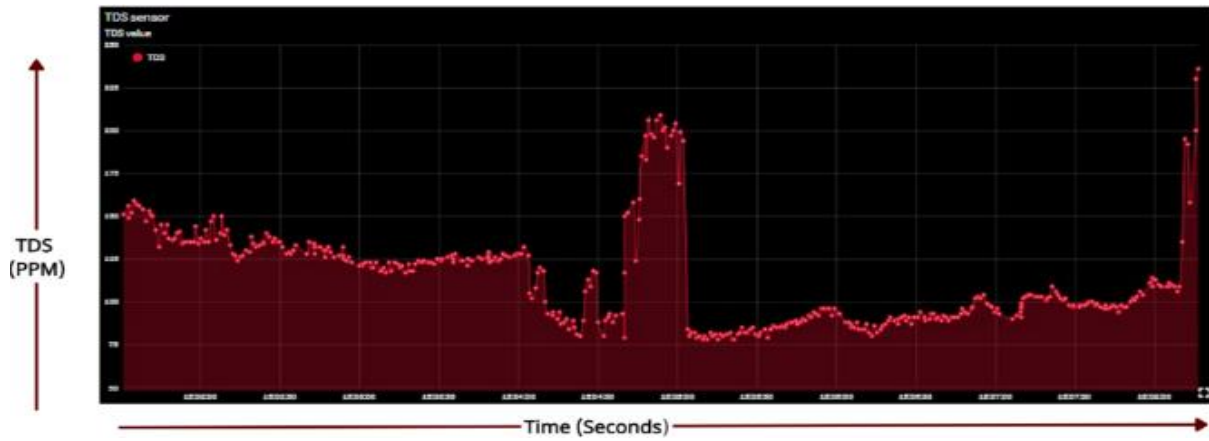
Fig. 11 Real-time graph for TDS.
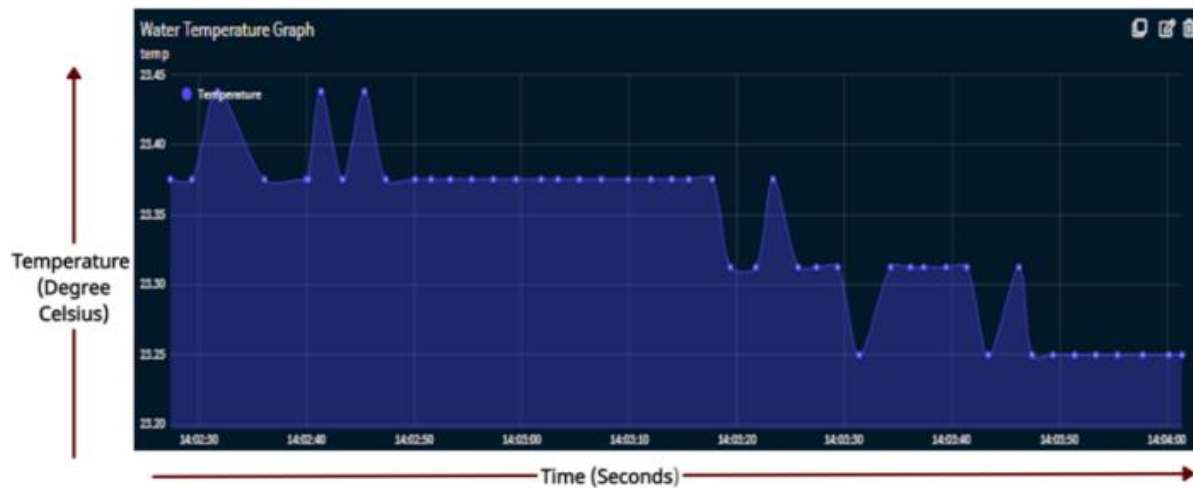
Fig. 12 Real-time graph of Temperature data

The figures given above represent the quality monitoring data of water parameters via visual and graphical representation while the gooch chart presents instant values. The experimental data are sent to the user's device for continuous monitoring of water quality and taking necessary action. Users can easily monitor the data received from sensors and control actuators with the help of a Graphical User Interface from any remote location. Thinger.io is used as an IoT platform for monitoring and controlling via a web server and an Android app. This device is connected to this interface via an IP address and the calibrated data is sent from the device. This Webserver and android Graphical user interface (GUI) is visible to the user from anywhere. It helps the user not only monitor the real-time data but also control the actuators using this app as well.

6 Conclusion

Biofloc Fish farming has been flourishing over recent years despite increasing prices, unavailability of workers, and the hassle of manual and regular water management. It is a crucial and exigent task to monitor the quality of water in a biofloc fish tank. The proposed automated and IoT based system can effortlessly and efficiently monitor the water quality parameters and does not need people on duty. It can be easily installed and located inside water. The smart system proficiently analyses and monitors the water quality data in real time while decreasing production costs and human reliance, enhancing productivity and sustainability. Also, the controlling device controls the air pump and temperature in accordance with the requirement. The entire system functions by an IoT based platform via a wireless network and send the monitored data very fast. By analyzing the received data, users can take action immediately. Future work of this research work involves including more sensors like dissolved oxygen sensors (DO) and ammonia sensors to monitor more parameters of water. The quality of water can be further predicted using a suitable machine learning algorithm as well.

References

[1] Crab, R., Defoirdt, T., Bossier, P. and Verstraete, W., 2012. Biofloc technology in aquaculture: beneficial effects and future challenges. *Aquaculture*, *356*, pp.351-356.

[2] Hargreaves, J.A., 2013. *Biofloc production systems for aquaculture* (Vol. 4503, pp. 1-11). Stoneville, MS: Southern Regional Aquaculture Center.

[3] Phawa, S.C., Ryntathiang, I., Shylla, W. and Das, G., 2020. Design and development of automation system for biofloc fish farming. *ADBU Journal of Electrical and Electronics Engineering (AJEEE)*, *4*(1), pp. 15-22.

[4] Mahajan, M., Kardile, A., Kasar, K. and Gaikwad, S., 2020. E-monitoring system for biofloc fish farming. *IJRAR-International Journal of Research and Analytical Reviews (IJRAR)*, *7*(2), pp. 653-657..

[5] Noor, M.Z.H., Hussian, A.K., Saaid, M.F., Ali, M.S.A.M. and Zolkapli, M., 2012, July. The design and development of automatic fish feeder system using PIC microcontroller. In *2012 IEEE Control and System Graduate Research Colloquium* (pp. 343-347). IEEE.

[6] Pathak, A., Tasin, A.H., Salma, U., Barua, L., Hossain, M.S. and Datta, S., IoT based low-cost system for monitoring water quality of karnaphuli river to save the ecosystem in real-time environment. *American Journal of Engineering Research, 9*(2), pp. 60-72.

[7] Parra, L., Sendra, S., García, L. and Lloret, J., 2018. Design and deployment of low-cost sensors for monitoring the water quality and fish behavior in aquaculture tanks during the feeding process. *Sensors*, *18*(3), p.750.

[8] Ramya, A., Rohini, R. and Ravi, S., 2019. IoT based smart monitoring system for fish farming. *International Journal of Engineering and Advanced Technology*, *8*(6 Special Issue), pp.420-424.

[9] Shaari, M.F., Zulkefly, M.E.I., Wahab, M.S. and Esa, F., 2011, August. Aerial fish feeding system. In *2011 IEEE International Conference on Mechatronics and Automation* (pp. 2135-2140). IEEE.

[10] Kayalvizhi, S., Reddy, G.K., Kumar, P.V. and Prasanth, N.V., 2015. Cyber aqua culture monitoring system using Ardunio And Raspberry Pi. *International Journal of Advanced Research in Electrical, Electronics and Instrumentation Engineering*, *4*(5), pp. 4554-4558.

[11] Chen, J.H., Sung, W.T. and Lin, G.Y., 2015, October. Automated monitoring system for the fish farm aquaculture environment. In *2015 IEEE International Conference on Systems, Man, and Cybernetics* (pp. 1161-1166). IEEE.

[12] Hendri, H., Enggari, S., Putra, M.R. and Rani, L.N., 2019, December. Automatic system to fish feeder and water turbidity detector using Arduino Mega. In *Journal of Physics: Conference Series* (Vol. 1339, No. 1, p. 012013). IOP Publishing.

[13] Lee, P.G., Turk, P.E., and Whitson, J.L., University of Texas System, 1999. Automated closed recirculating aquaculture filtration system and method. *U.S. Patent 5,961,831*.

[14] Garcia, M., Sendra, S., Lloret, G. and Lloret, J., 2011. Monitoring and control sensor system for fish feeding in marine fish farms. *IET Communications*, *5*(12), pp.1682-1690.

[15] Anuradha, T., Bhakti, C.R. and Pooja, D., 2018. IoT based low cost system for monitoring of water quality in real time. *Int. Res. J. Eng. Technol.(IRJET)*, *5*(5).

[16] Mozumder, S.A. and Sharifuzzaman Sagar, A.S.M., 2022. Smart IoT biofloc water management system using decision regression tree. In *Proceedings of International Conference on Fourth Industrial Revolution and Beyond 2021* (pp. 229-241). Springer, Singapore.

[17] Rashid, M., Nayan, A.A., Rahman, M., Simi, S.A., Saha, J. and Kibria, M.G., 2022. IoT based smart water quality prediction for biofloc aquaculture. *arXiv preprint arXiv:2208.08866*.

[18] Yang, X., Zhang, S., Liu, J., Gao, Q., Dong, S. and Zhou, C., 2021. Deep learning for smart fish farming: applications, opportunities and challenges. *Reviews in Aquaculture*, *13*(1), pp.66-90.

[19] Ahmed, U., Mumtaz, R., Anwar, H., Shah, A.A., Irfan, R. and García-Nieto, J., 2019. Efficient water quality prediction using supervised machine learning. *Water*, *11*(11), p.2210.

[20] Ahamed, I. and Ahmed, A., 2021, January. Design of smart biofloc for real-time water quality management system. In *2021 2nd International Conference on Robotics, Electrical and Signal Processing Techniques (ICREST)* (pp. 298-302). IEEE.

Temperature Effects on Optimal Performance of PV Module

Thomas Olabode Ale [1],*, Kayode Joel Rotipin[2], Tolulope David Makanju[3]

[1, 3]Department of Electrical and Electronics Engineering, Federal University of Technology, Ondo State, Nigeria
[2]Department of Mechanical Engineering, University of Ibadan, Oyo State, Nigeria

ABSTRACT

The commonly used renewable energy source (RES) is solar energy. However, the production of this energy from PV modules has a lot of challenges and still needs technological improvement. This research investigates the effects of temperature on Photovoltaic (PV) module optimal performance. An experimental setup of a Monocrystalline (MC) module was used and data on the temperature and other parameters were measured using appropriate measuring tools. The relationship between module temperature and other parameters was evaluated using Pearson product correlation. The findings of this study showed that the temperature is significant for the Monocrystalline PV module to operate at its optimal. Also, the finding revealed that there is a weak correlation between the open circuit voltage (OCV) of the panel and the temperature, however, the PV module temperature has a strong and positive correlation with other parameters namely; solar irradiance, short circuit current (SCC), output power and conversion efficiency (CE) with a correlation coefficient (CC) of 0.94, 0.93, 0.92 and 0.93 respectively. The conversion efficiency of the PV module increases when its temperature is within the maximum operating temperature and tends to decrease when the temperature is beyond the design operating temperature of the module. This implies that temperature is also a key parameter to consider when designing a PV module system for optimal performance. This research recommends that temperature should be considered in the design of PV modules to power any equipment or machines for better performance.

Keywords: Temperature, Photovoltaic, Efficiency, Correlation.

1 Introduction

Renewable energy sources (RES) have become a great way to alleviate the effect of climatic change on the environment. The trend in technology has paved way for the use of RES in most developed and developing countries which invariably serves as a way of sustaining the environment by reducing the dependence on nonrenewable sources of energy generation. However, this technology faced a lot of challenges in operating at its optimal performance [1]. One of the common RES aside from hydropower is solar energy (SE) which uses a solar PV module to convert sunlight directly to electricity [2]. Nnadi [3] studied the climatic effect on stand-alone solar energy supply performance for sustainable energy. The PV module was simulated on Matlab and the results were compared with other findings. The results of the research showed that the installation of a PV module away from obstruction enhanced the module's performance. However, the study did not state the relationship between temperature and operating parameters of the module in terms of correlation.

Also, the study of Tamunobereton-Ari [4] was focused on the influence of meteorological parameters on the efficiency of photovoltaic modules in some cities in the Niger Delta of Nigeria. The obtained results demonstrate that the solar flux and the output current were directly related to the solar panel efficiency. Additionally, the increased solar flux causes the output current of solar panels to rise, improving efficiency. Relative humidity was also seen to decrease the output current and boost efficiency. However, the researcher did not consider the effects of temperature on the PV parameters. Other reviewed literature [5]-[8] showed the effect of climatic and environmental factors such as ambient temperature, dirt and dust properties, shading, and acidic rain on the operation of the PV module in

their region. The review of the existing literature shows that the PV module is often characterized by its operating parameters in which any deviation can lead to alteration in the module operation. Some factors that affect the performance of the PV module are environmental factors such as shading and climatic parameters such as solar irradiance and temperature. The environmental factors can be eliminated through human intervention while the effect of the climatic parameters can be reduced to improve the performance of the PV module. One of the climatic parameters that can be reduced is the temperature because of its thermal degradation on the module, which affects the output power and other parameters of the PV module [9]. This research evaluated the effect of temperature on monocrystalline PV module operating parameters. The discovery of the PV effect by Edmond Becquerel in 1839, was not useful at that time until 10 decades later after Shockley had developed a model for the p–n junction, Bell Laboratories produced the first solar cell in 1954. One of the major challenging factors is the CE of PV modules which is relatively low 15-25 % [10]. When the solar irradiance fall on the PV module the hole and electron drift towards the p-n junction which will allow the flow of current and the ideal characteristics of the diode under dark condition is presented in Fig. 1. The output power of the PV module depends on the level of penetration of the solar irradiance that falls on the PV module and the CE of the module. Under normal operating conditions the higher the solar irradiance the higher the output power, however, variation in operating conditions will lead to alteration in the output characteristics of the module. Since the temperature of each region differs from one other and temperature is one of the parameters that determine other operating parameters of a PV module, due to its thermal effect on the module. There is a need to model the effect of temperature in Ibadan on monocrystalline

PV modules to know the effect of the temperature on PV that gives optimal performance.
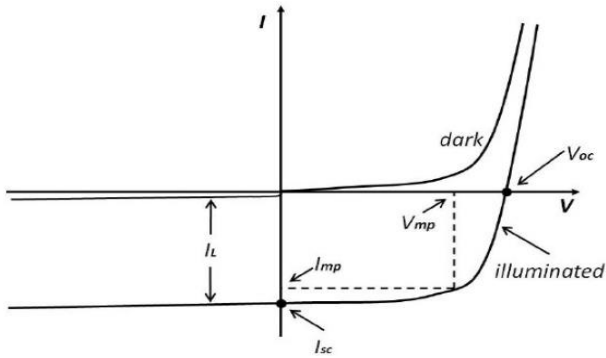
Fig. 1 I-V characteristics of an ideal diode solar cell when non-illuminated (dark) and illuminated.

2 Materials and Methods

An MC Photovoltaic module was set up from October (2017) to January (2018) at the University of Ibadan southwest Nigeria as presented in Fig. 2, with specifications shown in Table 1. The data was measured at 1hr intervals from 8 am in the morning till 6 pm in the evening with appropriate measuring instruments.

Fig. 2 View of the experimental setup.

The solar irradiance (W/m^2) incident on the surface was obtained using a solarimeter. Also, the Module temperature was measured with a k-type thermocouple temperature data logger. The voltage and current were determined using two different multimeters.

Table 1 PV Module specifications

Parameters	Value
Maximum power	150W
Maximum power tolerance	3%
(OCV)	23.1V
SCC	8.99A
Maximum power voltage	18V
Maximum power current	8.34A
Dimension (mm)	1480 by 670 by 30
Maximum system voltage	1000V
Maximum Overcurrent protection rating	15A
Module Application Class	A

The maximum power supplied by the PV module was computed using Eq. (1).

$$P = IV \qquad (1)$$

where I is the current and V is the voltage.

Pearson's correlation between the module temperature and other parameters was computed using Eq. (2).

$$r = \frac{\sum_{i=1}^{n}(t - \bar{t})(p - \bar{p})}{\sqrt{\sum_{i=1}^{n}(t_i - \bar{t})^2}\sqrt{\sum_{i=1}^{n}(p_i - \bar{p})^2}} \qquad (2)$$

where t is the temperature, $\bar{t}$ is the mean of temperature, p stand for other PV parameters considered such as OCV, current, solar irradiance, output power, and CE $\bar{p}$ is the mean of other parameters, i is the instant data while n is the sample size of the data. The photoelectric CE was calculated using equation (3).

$$\eta = \frac{P_{max}}{G \times A} \qquad (3)$$

where η is the photoelectric CE, G is the solar irradiance incident on the PV module, A is the surface area of the PV module, and P_{max} is the maximum power generated from the PV module.

3 Results and Discussion

The results of the study are presented in Table 2 and Fig. 3-Fig. 7. Fig. 3, shows that as the module temperature increases, the OCV is slightly increasing when the module temperature was within the range of 27.7℃ − 48.6℃. The OCV is maximum (20.6V) at a temperature of 36.6℃. The correlation coefficient between temperature and OCV in Table 1, suggests that there is a poor relationship between OCV and the temperature of the module. Also, with R-square value of 0.0656 implies only 6.5% of the observed data can be explained by the model. This implies that temperature can only explain its effect on voltage to an accuracy of 6.5%.
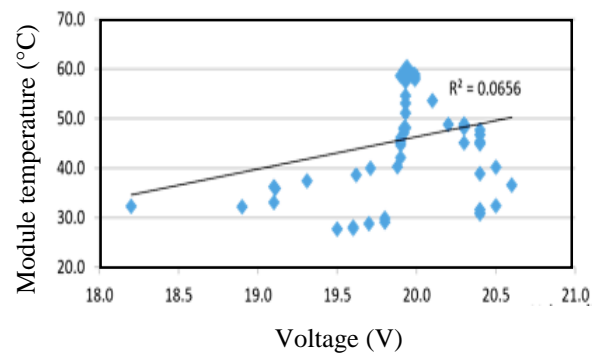
Fig. 3 The relationship between module temperature and voltage.

Table 2 Correlation results between temperature and other module parameters.

Parameter	R^2	Comments
OCV	0.256	Poor
Current	0.930	Strong
Solar Irradiance	0.938	Strong
Output Power	0.923	Strong
Conversion Efficiency	0.925	Strong

Fig. 4 shows the short circuit current also increases due to variations in temperature within the normal operating condition of the module. Also with a CC of 0.93, it implies that current and temperature have a strong and positive correlation. The R-square of 0.8648 in the model suggests that temperature can affect the current of a module up to 86.58%.

Fig. 5, shows a direct relationship between the module temperature and solar irradiance, and a CC of 0.938 implies that there is a strong relationship between the temperature module and solar irradiance. The R-square value of 0.8792 shows that temperature can affect the output power of the module up to 87.92%.

The relationship of module temperature with output power was observed as shown in Fig. 6, which indicates that as the temperature varies the output power increases and there is a strong relationship between the two variables as the CC is 0.923. At the peak temperature of 60°C, the maximum power was obtained. The R-square value of 0.8514 shows that temperature can affect the output power of the module up to 85.14%. This implies that the MC module subjected to a temperature of 60°C can give the maximum power output. This is against the study of [11] which states that solar modules perform better under a laboratory condition of 1000 W/m^2 incident solar irradiance, 25°C cell temperature. The temperature for the optimal performance for the monocrystalline PV module in Ibadan is 60°C.
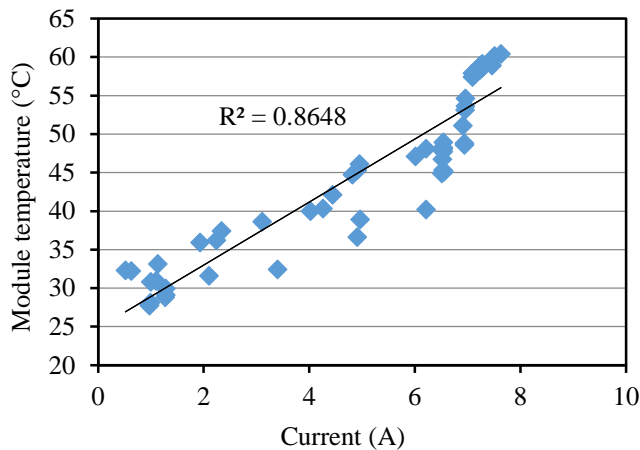
Fig. 4 The relationship between module temperature and Current
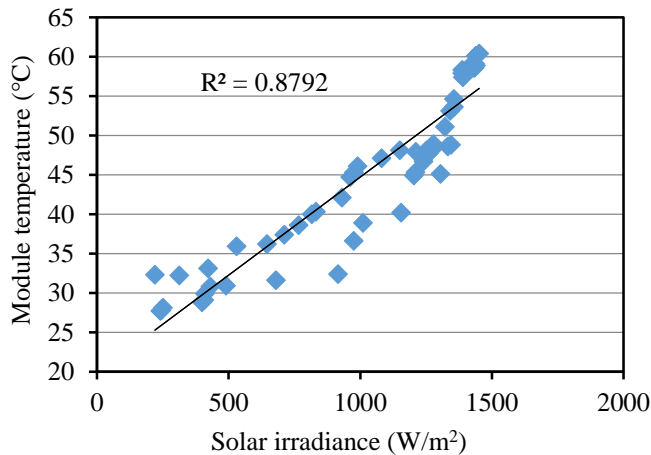
Fig. 5 The relationship between module temperature and solar irradiance
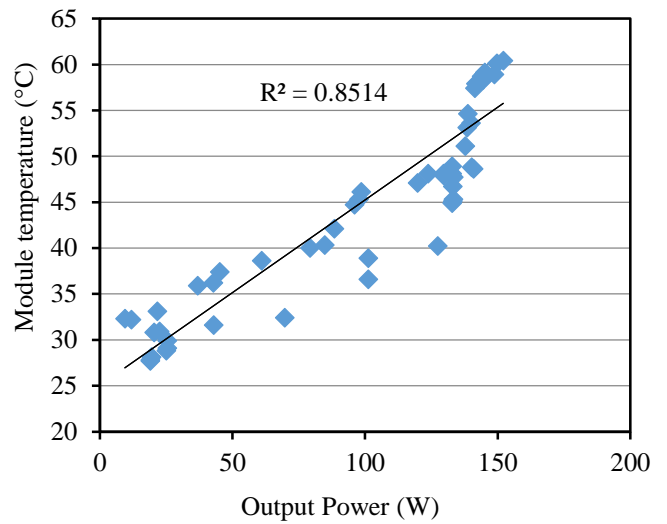
Fig. 6 The relationship between module temperature and output Power.

The results in Fig. 7, indicate that an increase in module temperature within the operating temperature limits leads to an increase in CE. The CE reaches a maximum of 15.4% when the module temperature is at a maximum of 60°C. This implies that the CE will continue to increase as the module temperature is within the operating limit. Also, the CC shows a strong relationship between the PV module temperature and output efficiency which shows that CE also depends on the module temperature. The R-square value of 0.8556 shows that temperature can affect the efficiency of the module up to 85.56%.
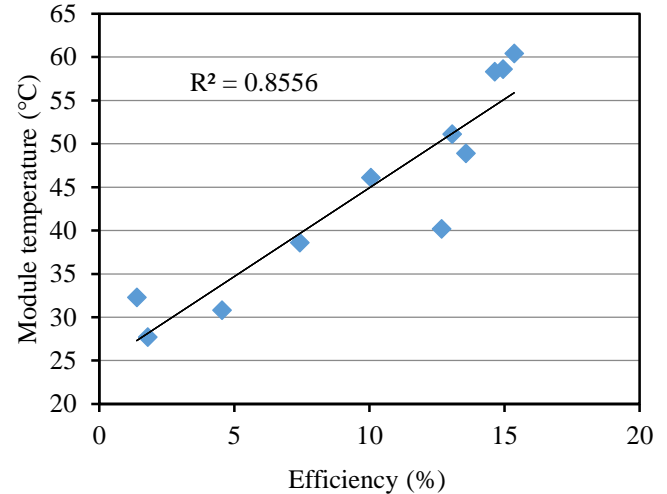
Fig. 7 Relationship between module temperature and efficiency

4 Conclusion

The research has shown that PV module temperature among other factors, has a great effect on PV performance. The findings of this study show that the PV module temperature has a positive and strong correlation with other parameters (Solar irradiance, short circuit current, output power, and CE). The temperature has a significant effect on the PV parameters to improve the performance of the PV module. Also, the study shows that the optimal temperature for the monocrystaline module in the study location is 60°C. This implies that temperature should be considered in the design of PV modules to power any equipment or machines for better performance.

References

[1] Ale, T.O. and Rotipin, K.J., 2019. Cooling effects on photovoltaic module performance in the tropical region. *Nigerian Journal of Technology*, *38*(3), pp.702-706.

[2] Makanju T.D. and Oluwalana O.J., 2020. A Novel Methodology For Modelling PV Module Based On Monitored Data. *Journal of Multidisciplinary Engineering Science Studies*, *6*(3), pp. 3072-3076.

[3] Nnadi, D.B.N., 2012. Environmental/climatic effect on stand-alone solar energy supply performance for sustainable energy. *Nigerian Journal of Technology*, *31*(1), pp.79-88.

[4] Tamunobereton-Ari, I., 2013. Influence of meteorological parameters on the efficiency of photovoltaic module in some cities in the Niger delta of Nigeria. *Journal of Asian Scientific Research*, *3*(1), pp. 107-113.

[5] Nobre, A., Montenegro, A., Zhen, Y., Reindl, T. and Ruther, R., 2012. On PV Module Temperature in Tropical Region-a Comparison between System Locations in Singapore and Brazil. In *IV Congresso Brasiliero de Energia Solar eV Conferencia Latino-Americana de ISES* (pp. 1-8).

[6] Samadhiya, A. and Pandey, R., 2016. Analysis of PV panels under various weather conditions. *International Journal of Emerging Research in Management & Technology*, *5*(2), pp. 53-61.

[7] Bioudun, A.D., Kehinde, A.D., and Aminat, O.T., 2017. Experimental evaluation of the effect of temperature on polycrystalline and monocrystalline photovoltaic modules. *IOSR Journal of Applied Physics*, *9*(2), pp.5-10.

[8] Setiawan, E.A., 2017. Analysis on solar panel performance and PV-inverter configuration for tropical region. *Journal of Thermal Engineering*, *3*(3), pp. 1259-1270.

[9] Amelia, A.R., Irwan, Y.M., Leow, W.Z., Irwanto, M., Safwati, I. and Zhafarina, M., 2016. Investigation of the effect temperature on photovoltaic (PV) panel output performance. *Int. J. Adv. Sci. Eng. Inf. Technol*, *6*(5), pp. 682-688.

[10] Musthafa, M.M., 2015. Enhancing photoelectric conversion efficiency of solar panel by water cooling. *Journal of Fundamentals of Renewable Energy and Applications*, *5*(4), pp. 1-5.

[11] Adeeb, J., Farhan, A. and Al-Salaymeh, A., 2019. Temperature effect on performance of different solar cell technologies. *Journal of Ecological Engineering*, *20*(5), pp. 249-254.

This page is left intentionally blank

Indexed by:

Google Scholar | Crossref

Scilit

.